Title

Microglia orchestrate tumor suppressive activity and upregulate antigen presentation machinery in the early-stage response to breast cancer brain metastasis.

Author

Longworth, Aaron Jacob

Publication Date

2023

UNIVERSITY OF CALIFORNIA,
IRVINE

Microglia orchestrate tumor suppressive activity and upregulate antigen presentation machinery in the early-stage response to breast cancer brain metastasis.

DISSERTATION

submitted in partial satisfaction of the requirements
for the degree of

DOCTOR OF PHILOSOPHY

in Biomedical Sciences

by

Aaron Jacob Longworth

Dissertation Committee:
Associate Professor Devon A. Lawson, Chair
Professor Thomas E. Lane
Professor Mathew Blurton-Jones
Assistant Professor Francesco Marangoni
Assistant Professor Lisa Wagar

2023

DEDICATION

To

Alyssa, Jackie, and little Logan

“For the first time in longer than I can remember, I feel peaceful. Not happy. Not sad. Not anxious. Just all the higher parts of my brain closing up shop. The cerebral cortex. The cerebellum. That's where my problem is. I'm now simplifying myself. Somewhere balanced in the perfect middle between happiness and sadness. Because sponges never have a bad day.”
— Chuck Palahniuk
Choke

TABLE OF CONTENTS

LIST OF FIGURES

ACKNOWLEDGEMENTS

I would like to express my sincerest appreciation to my mentor and dissertation committee chair, Dr Devon A Lawson, for her unwavering dedication to critical, impactful science and progress to inform patient care and quality of life. I would furthermore like to thank my esteemed committee for their thoughtful insight, encouragement, and for fostering an unparallelled academic community in immunology, neuroimmunology, and immuno-oncology at the University of California, Irvine. *Fiat Lux*.

Portions of Chapter 1 of this text is a reprint of the material as it appears in the following publication:

Evans, K.T., Blake, K., Longworth, A. *et al.* Microglia promote anti-tumour immunity and suppress breast cancer brain metastasis. *Nat Cell Biol* (2023). https://doi.org/10.1038/s41556-023-01273-y

used with permission from Springer Nature. The co-authors listed in this publication are as follows:

Katrina T. Evans, Kerrigan Blake, Morgan A. Coburn, Jacob Insua-Rodríguez, Timothy P. McMullen, Quy H. Nguyen, Dennis Ma, Tatyana Lev, Grace A. Hernandez, Armani K. Oganyan, Davit Orujyan, Robert A. Edwards, Clare Pridans, Kim N. Green, S. Armando Villalta, Mathew Blurton-Jones & Devon A. Lawson

Portions of Chapter 2 of this text is a reprint of the material as it appears in the following publication:

Evans, K.T., Blake, K., Longworth, A. *et al.* Microglia promote anti-tumour immunity and suppress breast cancer brain metastasis. *Nat Cell Biol* (2023). https://doi.org/10.1038/s41556-023-01273-y

used with permission from Springer Nature. The co-authors listed in this publication are as follows:

Katrina T. Evans, Kerrigan Blake, Morgan A. Coburn, Jacob Insua-Rodríguez, Timothy P. McMullen, Quy H. Nguyen, Dennis Ma, Tatyana Lev, Grace A. Hernandez, Armani K. Oganyan, Davit Orujyan, Robert A. Edwards, Clare Pridans, Kim N. Green, S. Armando Villalta, Mathew Blurton-Jones & Devon A. Lawson

Portions of Chapter 3 of this text is a reprint of the material as it appears in the following publication:

Evans, K.T., Blake, K., Longworth, A. *et al.* Microglia promote anti-tumour immunity and suppress breast cancer brain metastasis. *Nat Cell Biol* (2023). https://doi.org/10.1038/s41556-023-01273-y

used with permission from Springer Nature. The co-authors listed in this publication are as follows:

Katrina T. Evans, Kerrigan Blake, Morgan A. Coburn, Jacob Insua-Rodríguez, Timothy P. McMullen, Quy H. Nguyen, Dennis Ma, Tatyana Lev, Grace A. Hernandez, Armani K. Oganyan, Davit Orujyan, Robert A. Edwards, Clare Pridans, Kim N. Green, S. Armando Villalta, Mathew Blurton-Jones & Devon A. Lawson

Portions of Chapter 4 of this text is a reprint of the material as it appears in the following publication:

Evans, K.T., Blake, K., Longworth, A. *et al.* Microglia promote anti-tumour immunity and suppress breast cancer brain metastasis. *Nat Cell Biol* (2023). https://doi.org/10.1038/s41556-023-01273-y

used with permission from Springer Nature. The co-authors listed in this publication are as follows:

Katrina T. Evans, Kerrigan Blake, Morgan A. Coburn, Jacob Insua-Rodríguez, Timothy P. McMullen, Quy H. Nguyen, Dennis Ma, Tatyana Lev, Grace A. Hernandez, Armani K. Oganyan, Davit Orujyan, Robert A. Edwards, Clare Pridans, Kim N. Green, S. Armando Villalta, Mathew Blurton-Jones & Devon A. Lawson

Portions of Chapter 6 of this text is a reprint of the material as it appears in the following publication:

Evans, K.T., Blake, K., Longworth, A. *et al.* Microglia promote anti-tumour immunity and suppress breast cancer brain metastasis. *Nat Cell Biol* (2023). https://doi.org/10.1038/s41556-023-01273-y

used with permission from Springer Nature. The co-authors listed in this publication are as follows:

Katrina T. Evans, Kerrigan Blake, Morgan A. Coburn, Jacob Insua-Rodríguez, Timothy P. McMullen, Quy H. Nguyen, Dennis Ma, Tatyana Lev, Grace A. Hernandez, Armani K. Oganyan, Davit Orujyan, Robert A. Edwards, Clare Pridans, Kim N. Green, S. Armando Villalta, Mathew Blurton-Jones & Devon A. Lawson

Portions of Chapter 7 of this text is a reprint of the material as it appears in the following publication:

Evans, K.T., Blake, K., Longworth, A. *et al.* Microglia promote anti-tumour immunity and suppress breast cancer brain metastasis. *Nat Cell Biol* (2023). https://doi.org/10.1038/s41556-023-01273-y

used with permission from Springer Nature. The co-authors listed in this publication are as follows:

Katrina T. Evans, Kerrigan Blake, Morgan A. Coburn, Jacob Insua-Rodríguez, Timothy P. McMullen, Quy H. Nguyen, Dennis Ma, Tatyana Lev, Grace A. Hernandez, Armani K. Oganyan, Davit Orujyan, Robert A. Edwards, Clare Pridans, Kim N. Green, S. Armando Villalta, Mathew Blurton-Jones & Devon A. Lawson

Research reported in this publication was supported by the National Institute of Health/ National Cancer Institute award number R01CA237376-01A1, to DAL., the American Cancer Society award number IRG-98-279-10 to DAL, the Center for Complex Biological Systems, University of California, Irvine NIH/NCI U54-CA-217378 to DAL and MBJ, the National Institutes of Health award T32NS121727-01 to AL, the National Institutes of Health T32AI 0602573, the Stanley Behrens Fellows in Medicine award and the UCI Graduate Dean's Dissertation Fellowship to KTE, the National Institute of Health award number NIHT32EB009418 and the UCI Public Impact Fellowship to KB, the National Institute of Neurological Disorders, Stroke/ National Institutes of Health under award number T32NS082174 to MAC, the Canadian Institutes of Health Research Postdoctoral Fellowship to DM, and the National Institutes of Health T32GM136624 and F31CA281331 to TL. The author wishes to acknowledge the support of the Chao Family Comprehensive Cancer Center Experimental Tissue Shared Resource, supported by the National Cancer Institute of the National Institutes of Health under award number P30CA062203. The

funders had no role in study design, data collection and analysis, decision to publish or preparation of the manuscript. This research is solely the responsibility of the authors and does not necessarily represent the official views of the National Institutes of Health.

VITA

Aaron Jacob Longworth

2002-04	Nuclear Prototype Instructor, Naval Nuclear Prototype Training Command, United States' Navy
2004	Master Training Specialist, United States' Navy
2004-08	Reactor Machinery Lead Planner, USS Ronald Reagan, United States' Navy
2013	Undergraduate Researcher, DerMardirrosian Lab, The Scripps Research Institute
2014	B.S. in Physiology and Neuroscience, University of California, San Diego
2015-19	Scientist – Cancer Vaccines & Immunotherapeutics, Pfizer
2023	Ph.D. in Biomedical Sciences, University of California, Irvine

FIELD OF STUDY

Immuno-oncology and Neuroimmunology

PUBLICATIONS

1. Evans K[1], Blake K[1], **Longworth A[1]**, et al. Microglia promote anti-tumor immunity and suppress breast cancer brain metastasis. Nat Cell Biol. 2023 Nov 13. doi: 10.1038/s41556-023-01273-y. Epub ahead of print. PMID: 37957324
2. **Longworth A**, Evans K…, Lawson DA. Leveraging parenchymal antigen presentation of microglia for the control of breast cancer brain metastases. Poster presented at 38th annual meeting of the Society for Immunotherapy in Cancer, San Diego, CA, USA. November, 2023.
3. **Longworth A,** Mallya S…, Lawson DA. Multiomic and spatial immunophenotyping reveals a prominent Runx3$^+$ resident T cell population in the healthy human breast. J Immunol 1 May 2023; 210 (1_Supplement): 63.12. https://doi.org/10.4049/jimmunol.210.Supp.63.12
4. **Longworth A**, Evans K…, Lawson DA. In situ analysis of the metastatic immune milieu in breast cancer brain metastasis at the single-cell level. J Immunol 1 May 2022; 208 (1_Supplement): 179.01. https://doi.org/10.4049/jimmunol.208.Supp.179.01
5. Ma D, Hernandez GA…, **Longworth A**, et al. Patient-derived xenograft culture-transplant system for investigation of human breast cancer metastasis. Commun Biol 4, 1268 (2021). https://doi.org/10.1038/s42003-021-02596-y
6. Josic M[1], **Longworth A**[1]…, Martinic M. Differential impact of chemotherapy on tumor-associated antigen-specific immunogenicity in cynomolgus macaques. Poster presented at 32nd annual meeting of the Society for Immunotherapy in Cancer, National Harbor, MD, USA. November, 2017.

ABSTRACT OF THE DISSERTATION

Microglia orchestrate tumor suppressive activity and upregulate antigen presentation machinery in the early-stage response to breast cancer brain metastasis.

by

Aaron Jacob Longworth

Doctor of Philosophy in Biomedical Sciences

University of California, Irvine, 2023

Professor Devon A. Lawson, Chair

Breast cancer brain metastasis (BCBM) is an increasingly prevalent clinical problem, due largely to improvements in treatment of primary tumors. Incidence of BCBM is rapidly fatal and difficult to treat, owing to the relative impermeability of the blood-brain barrier (BBB) to standard-of-care treatments and restrictions on the influx of peripheral immune cells during tumor initiation. As the resident macrophage and predominant immune cell of the central nervous system (CNS), microglia are poised to be the first responders to metastatic tumor infiltration, however an accumulating body of literature implies that microglia facilitate tumor growth in the CNS and brain parenchyma. In the following studies, we employ single-cell RNA sequencing (scRNAseq), spatial immunophenotying and flow cytometry on murine models of BCBM to interrogate the CNS immune microenvironment during tumor initiation to evaluate the tumoricidal potential of microglia and evaluate modalities for treatment of intracranial metastases. We identify the emergence of a pro-inflammatory program in microglia upon incidence of BCBM consistent with the canonical activity of a tumoricidal macrophage. We subsequently demonstrate that microglia upregulate antigen presentation (AP) machinery, and this activity is largely dependent on the infiltration of lymphocytes from the periphery. Finally, we evaluate the impact of agonistic anti-CD40 antibody on AP activity and the capacity to clear BCBM lesions.

INTRODUCTION

Breast cancer brain metastasis (BCBM) is increasing in incidence and rapidly emerging as a critical clinical problem in breast cancer. 15-30% of metastatic breast cancer patients develop brain metastasis, and autopsy and imaging studies indicate an additional 30% of patients are likely to develop brain metastasis as treatments for peripheral disease improve and patients live longer[1,2]. This is particularly alarming, considering there are no effective treatments for brain metastasis and median survival is a paltry few months[3–6]. There is growing interest in immunotherapeutic strategies to treat central nervous system (CNS) cancers, given that immune cells enter the brain during disease while most conventional therapies are excluded by the blood brain barrier (BBB)[7,8]. However, greater understanding of the immune response to BCBM will be needed to develop immunotherapy strategies effective in the unique immune microenvironment of the CNS.

The brain immune microenvironment is principally composed of specialized tissue resident macrophages, known as microglia, that tile the brain and play diverse functions in CNS homeostasis and disease[9–11]. Microglia represent an attractive immunotherapeutic target because they are the first line of defense to disease in the CNS and have the power to direct the initial immune response. BCBMs are heavily infiltrated with tumor associated macrophages (TAMs), which may be comprised of microglia, border-associated macrophages (BAMs), as well as bone marrow derived myeloid cells (BMDMs) such as monocytes and macrophages[12–16]. Functional studies using genetic and pharmacologic approaches to deplete TAMs suggest a tumor promoting role for these cells. Depletion of TAMs with CSF1R inhibitors results in tumor reduction and decreased metastasis in glioblastoma and melanoma models[17–21]. TAM depletion using a CX3CR1-targeted genetic ablation model similarly results in decreased BCBM[22]. However, it is unclear whether microglia or other types of TAMs produce the tumor promoting effects observed in these studies. CSF1R inhibitors have been shown to preferentially deplete microglia, but also attenuate other myeloid cells, and microglia ultimately repopulate the brain when treatment ceases.

Likewise, CX3CR1 is expressed by diverse myeloid cell populations and upregulated by BMDMs upon entry into the brain[23]. Therefore, the specific impact of brain resident microglia on tumor initiation and their potential as an immunotherapy target remain unclear.

In the following studies, we combined single cell RNA-sequencing (scRNA-seq) with newly developed genetic and humanized mouse models to find that microglia suppress BCBM by promoting anti-tumor NK and T cell responses. ScRNA-seq of >90,000 cells from three different BCBM models revealed that microglia mount a robust pro-inflammatory response to BCBM, characterized by upregulation of three core programs for IFN response, antigen presentation (AP), and secretion of inflammatory mediators. Using a genetic knockout model, we find that animals lacking microglia show increased metastasis, decreased survival, and impaired NK and T cell responses to BCBM[24]. We show that ablation of T cells shifts microglia activation and attenuates their tumor suppressive effect, indicating that reciprocal microglia-T cell activation is critical to suppress BCBM. Utilizing a humanized mouse model, we further find that the pro-inflammatory response is conserved in human microglia, and analysis of patient BCBM data indicates that increased proinflammatory marker expression is associated with better prognosis. These findings contrast with the pro-tumorigenic function reported for TAMs and highlight the potential of harnessing the antitumor function of microglia to treat brain metastasis.

Literature Review:

While advancements in early detection and treatment of breast cancer have drastically improved patient survivability and quality of life in the last 40 years, incidence of brain metastasis and the resulting mortality has been steadily increasing[1,2]. This is largely attributed to the expanded life expectancy due to novel treatment modalities, such as the advent of immunotherapy, but it remains that these treatments are not universally effective nor are approved therapies capable of infiltrating the CNS[1, 3-7]. It therefore stands to reason that there is a drastic unmet need for therapies that are capable of not only combatting tumor indications that may infiltrate the brain, but also eliciting an effect across the BBB. Options for such treatment include use of BBB permeable lipophilic small molecules, typically fewer than 600 Da, direct delivery of treatment agents to the brain parenchyma through transmeningeal or intrathecal injections, or the chaperoning of peripheral agents across the BBB, each of whom come with their own complications[25-29]. As such, it is imperative that we understand orchestration of the immune response to BCBM, the key players and bad actors, as well as common misconceptions in the brain tumor immune response and opportunities for treatment intervention.

Historically, the brain has largely been considered and immune-privileged site, much like the eye, testes, and placenta during pregnancy; an immunological desert where the body has evolutionarily excluded the infiltration of leukocytes to prevent the potential havoc a cytolytic and inflammatory response could cause. Upon discovery in 1919, microglia, the most abundant immune cells in the brain, were originally considered connective tissue[30]. Shortly thereafter, their phagocytic activity had them upgraded to functional glial cells as we began to understand the role in the clearance of parenchymal debris, however only identified for their immunogenic potential upon the discovery of AP activity in 1986[31]. Nonetheless, the function of microglia is still predominately researched in the context of brain maintenance, learning and memory, and neurodegeneration as opposed to their capacity to drive the immune response and clear pathogens. The advent of genomic and multiomic data, particularly at the single cell level, has shifted the understanding of the role of microglia to that of specialized, CNS-tissue resident macrophages with diverse functionality in a plethora of homeostatic and disease states[32].

Microglia are yolk-sac derived resident macrophages of the CNS, akin to the Langerhans cells of the skin or Kuppfer cells of the liver, that develop in the early embryo and persist into adulthood memory[33, 34]. They appear to be replenished locally through the existing population as evidenced through chimeric models derived by parabiosis; they have been demonstrated not to be haematopoietically derived in the manner of peripheral macrophages, however the definitive source of microglia replenishment in adulthood remains under heated debate[34]. Their activity has primarily been studied in the context of CNS tissue homeostasis, learning, and memory, and their function in health predominantly lies within that bailiwick. In steady state, microglia exhibit a ramified morphology and survey the brain parenchyma through the extension of processes for neuronal synaptic activity or damage and inflammatory stimuli[35, 36]. These interactions inform microglia to perform their maintenance functions within the CNS of synaptic pruning and organization, control of neuronal excitation, clearance of debris, and protection and repair of the brain[37]. Upon receipt of an inflammatory stimulus through recognition pathogen- and damage- associated molecular patterns (PAMPs, DAMPs) microglia adopt an amoeboid structure, proliferate, and upregulate phagocytic activity and pro-inflammatory signaling [25, 38, 39].

Macrophages, and by extension microglial activity has historically been compartmentalized into an “M1” versus “M2” dichotomy; more specifically, M1 macrophages carry out classic inflammatory function increasing cytotoxicity through the production of free radicals (Reactive oxygen species, nitrogen reactive species) and inflammatory cytokines (interleukin-12 [IL-12], tumor necrosis factor alpha [TNFa]) while M2 alternative macrophages are involved in tissue maintenance and repair and release immunosuppressive cytokines (IL-10 and transforming growth factor-beta [TGFb]) and growth factors such as fibroblast growth factor and colony stimulating factor 1 (CSF-1)[40]. It is widely recognized that this binning of microglia activity is a drastic oversimplification, however the nomenclature remains a useful descriptor, particularly in summarizing the activity of microglia and other macrophages in the context of immuno-oncology. It is well reported that tumors are notoriously capable of immune evasion[41, 42, 43] and one of the key mechanisms of this is the M2 polarization of tumor-associated macrophages (TAMs).

Microglia are no exception to tumor induced immunosuppressive polarization; much of recent literature in primary and metastatic tumors in the CNS leans into this phenomenon[17-21]. Current understanding of the myeloid immune milieu poorly differentiates TAMs derived from peripheral monocyte derived macrophages, microglia, and non-microglia, CNS resident macrophages. This generalization is understandable, as there are minimal differentiators between these subtypes including few transcriptional markers, fewer surface proteins, and morphological differences only observable with low-throughput imaging techniques that obscure more robust data [36, 40]. Most depletion strategies rely on blocking microglia survival signaling through the CSF-1 Receptor (CSF1R) that is expressed on all macrophage subtypes, or through genetic manipulation driven by CX3XR1 expression, which is not entirely specific to microglia[17, 44]. Alternative mouse models have been developed utilizing the Tmem119, P2ry12, and Hexb promoters which are more specific to microglia, but results, particularly involving the requisite expression of a Cre recombinase for gene locus excision, have been middling at best[45]. As it stands, experimental conclusions in neuroimmunology must be drawn from consistent results in multiple diverse models until a more robust method of depletion and germline modification of microglia is validated.

The overwhelming majority of the work performed in brain tumors, particularly those investigating microglial activity, is performed in primary brain tumors (glioma, glioblastoma), but treatment of metastasis has a distinct immunological advantage: education of the adaptive immune response on a peripheral primary tumor. It is only in relatively recent understanding that thymic-derived T cells, the *de facto* effectors of the adaptive immune response, may be recruited to the CNS to perform cytolytic activity[46]. The exclusion of T cells is largely apparent in homeostasis, where the absence of non-self peptides sufficient to provoke an immune response result in a near complete omission of a T cell repertoire. This exclusion is almost wholly attributed to the tight regulation of trafficking into the parenchyma by the BBB, a tight network of endothelial and accessory cells separating the CNS from the periphery[47]. Paracellular vascular permeability is regulated by dynamic tight junctions that largely exclude the infiltration of foreign and superfluous bodies but license necessary cells and compounds to enter as necessary. The purpose of such tight regulation is manifold: the brain is provided a hard volume limit imposed by the cranium therefore inflammation induced swelling can become rapidly problematic, uncontrolled and nonspecific ligation and modulation of CNS receptors can cause a multitude of unintentional effects, and the intrusion of pathogenic virus or bacteria can cause irreparable damage to the host. This presents monumental challenges to the treatment of intracranial pathology such as BCBM or any number of neurodegenerative diseases[48, 49, 50].

T cell infiltration was initially and most predominantly observed in Experimental Autoimmune Encephalomyelitis (EAE), a murine model of Multiple Sclerosis (MS), where autoreactive T cells specific to proteins in the myelin sheath of neurons, infiltrate the brain parenchyma and cause extensive damage to myelinated cells[51, 52]. In this case, the site of T cell activation remains unclear. Evidence of CNS peptide presentation by antigen presenting cells (APCs) to T cells had been observed in the draining cervical lymph nodes (LNs), the meninges, and by microglia in the parenchyma, but the relative impact of AP at each site on the whole of the immune response remains elusive[53, 54, 55]. This facet of the immune response to EAE, much like that of Alzheimer's disease, more specifically informs that of the anti-tumor response in the CNS than viral or bacterial infection, as the tumor is comprised of endogenous or mutated self antigens[56]. These antigens are presumably lowly or nonimmunogenic due to the negative selection of self-reactive T and B cells in lymphocyte development, and where the source of aberrant T cell specificity in MS and EAE remains unclear, it is similarly obscured in the response to CNS tumors. In the case of BCBM, the adaptive T cell repertoire benefits from the existence of a peripheral tumor, however it remains that brain metastasis is a nearly certain cause of mortality[1,2]. To identify points of failure in the immune response to BCBM, we must first wholly understand the activity of the CNS resident immune repertoire.

Presently, standard-of-care treatment for brain metastasis is extremely limited, rarely curative and focused on maintaining an acceptable quality of life for the patient[57]. Surgical resection is considered the most promising but must be performed when known lesions are accessible and located where resulting damage will have minimal ancillary effects. Results, however, are most often successful when removing large sections of parenchymal legions is possible, vice piecemeal resection of micrometastases increasing the likelihood for complications[58]. Following resection or in cases where surgery is not feasible, whole brain radiotherapy (WBRT) is used and was previously considered the standard treatment. Retroactive studies on the efficacy of WBRT, however, show no appreciable benefit with a median survival of 3-6 months in patients without surgical resection, and treatment is often associated with severe neurocognitive dysfunction[59]. Stereotactic Radiosurgery (SRS) has emerged as a more effective targeted option and is increasingly being used where surgical resection isn't possible. SRS is the targeted administration of high-dose radiation at the site of the lesion and is the preferred method for lesions proximal to critical structures such as the brain stem[58]. While SRS as a monotherapy provided no significant difference in overall survival when compared to WBRT, post resection SRS demonstrated a freedom from local recurrence of metastatic lesions of 72% in SRS treated group vs. a

42% recurrence in resection alone[60]. While this is an important improvement in the treatment of BCBM, a drastic unmet need remains for more long-term and curative therapies.

The advent of checkpoint inhibition and immunotherapy, pioneered by the Nobel Prize winning discovery of PD-1 and CTLA-4 checkpoint blockade by James Allison and Tasuku Honjo, has been a tremendous boon to the treatment of cancer patients and, by extension, those with distal metastases[61]. Checkpoint blockade has been used with mild success in BCBM and brain metastasis from alternate sources, however it remains that checkpoint blockade is only successful in an undefined subset of cancer patients. Prognosis is improved with combination therapies, including multi agent immunotherapies and those involving radiation and chemotherapy, however the median survival in the most responsive, $HER2^+$ subtype of breast cancer is modestly improved from 5.6 to 7.8 months[1,2]. Current administration of immunotherapy is a systemic treatment, however most clinical trials for cancer immunotherapies explicitly exclude patients with progressive brain metastasis due to their poor prognosis, effectively ignoring the treatment potential of the most dire cancer indications[62, 63, 64]. Precedent exists in neurodegenerative disease for transmeningeal administration of drugs[26, 27], which may provide a more targeted effect to brain lesions, particularly considering the unique composition of the parenchymal immune repertoire of the brain.

The high instance of brain metastasis in late-stage breast cancer, paired with its relative resistance to treatment and dismal prognosis presents a clear opportunity for improved modalities of intervention. Progress in the treatment of BCBM necessitates a deeper understanding of the immune response at the onset of metastasis and throughout the progression of disease. While existing literature paints microglia in an unflattering light, research in neurodegeneration and infection exhibits a reliable proinflammatory capacity for microglia that might be leveraged for tumor control. By analyzing the activity of microglia and the CNS immune repertoire at the initiation of metastasis, we seek to identify points of failure in the antitumor immune response to inform opportunities for treatment intervention. In the following text, we interrogate the CNS immune milieu in BCBM to evaluate the progression of the antitumor immune response and postulate options for treatment modalities that may provide relief for a drastically underserved patient population.

Experimental Results:

Microglia display a robust pro-inflammatory response to BCBM

We investigated TAM infiltration in human and mouse BCBM by *in situ* immunofluorescence (IF) for ionized calcium-binding adaptor molecule 1 (IBA1)[25]. In normal human brain, IBA1$^+$ cells are evenly spaced and display ramified morphology typical of homeostatic microglia (Fig 1.1d). In contrast, patient BCBM shows heavy infiltration with IBA1$^+$ cells that display ameboid morphology typical of activated microglia and macrophages (Fig 1.1d). The MDA-MB-231-BR (231BR) model of mouse BCBM shows similar features (Fig 11.1a) In this model, GFP-labeled 231BR cells are delivered into arterial circulation of immune deficient animals via intracardiac injection, which facilitates metastasis to the brain (Fig 1.1a)[65,66]. Consistent with prior reports, we find that 231BR cells arrest in blood vessels and cross into the brain two to seven days after injection, then grow along blood vessels and form micrometastases by day 14 and parenchymal metastasis by day 28 (Fig 1.1b)[67,68]. Interestingly, IF analysis shows that IBA1$^+$ cells surround and directly interface with cancer cells by day seven, showing they interact with cancer cells at the initial stages of metastasis (Fig 1.1b). We further found that day 28 parenchymal metastases are densely infiltrated with IBA1$^+$ cells, in contrast to regions of normal tissue distal to metastases (1.95-

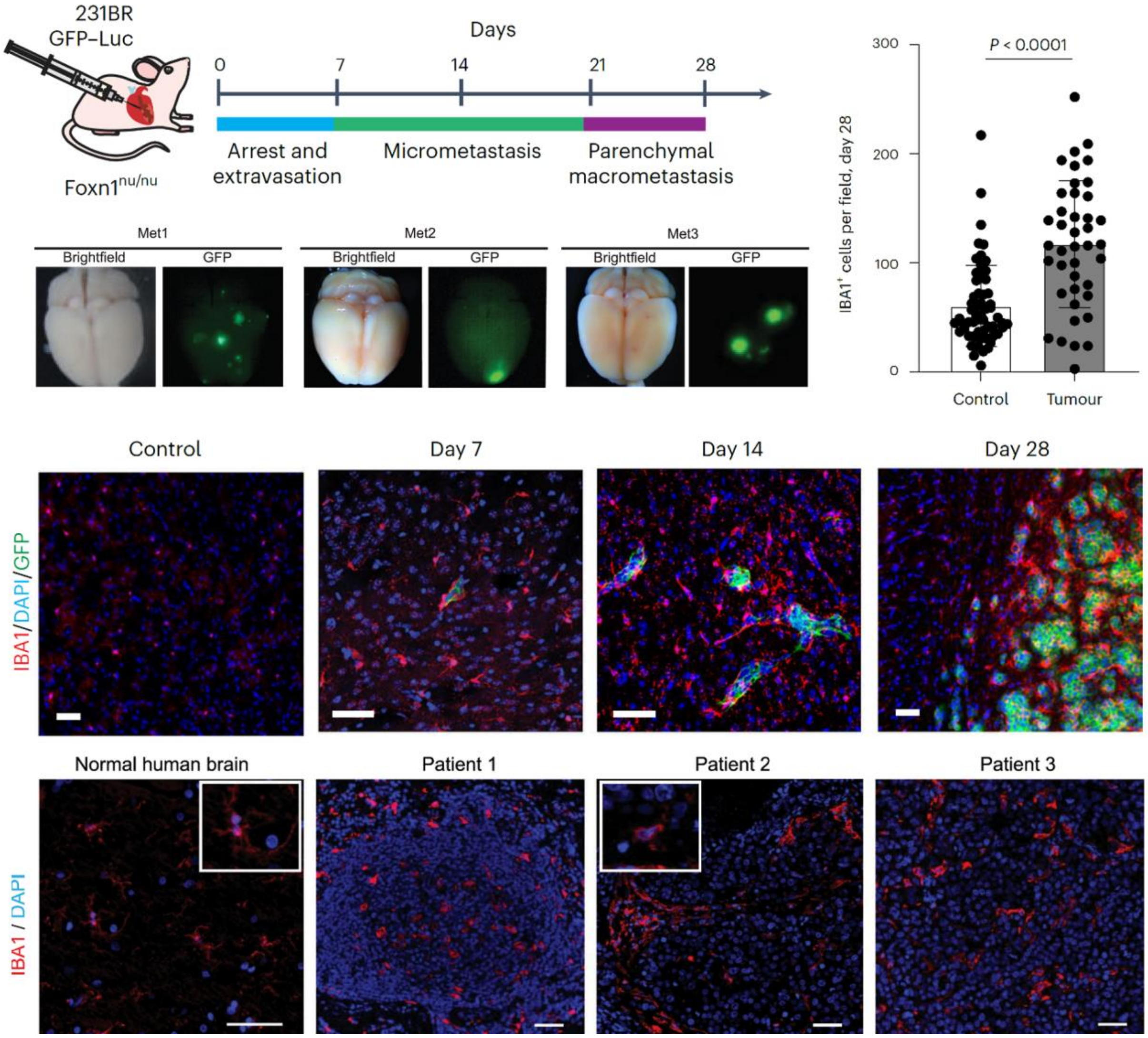

Figure 1.1. Microglia localize to tumor lesions in BCBM. **a**, Schematic showing disease progression in mouse 231BR–Foxn1nu/nu BCBM experimental metastasis model. A total of 500,000 GFP–Luc-labelled 231BR cells were injected into the left cardiac ventricle of Foxn1nu/nu mice and collected 28 days later. Whole-mount brightfield and fluorescence microscopy images show a representative brain with GFP$^+$ metastatic foci (green). **b**, IF staining showing IBA1$^+$ cells (red) in control and metastatic brains at 7, 14 and 28 days post 231BR cell injection. Metastatic cells are GFP$^+$ (green). 231BR cells arrest in blood vessels and cross into the brain 2–7 days post-injection, then grow along blood vessels forming micrometastases by day 14, parenchymal metastases by day 28. Scale bar, 50 µm. **c**, Quantification of IBA1$^+$ cells in control (n = 4) and metastatic (n = 4) brains 28 days post 231BR cell injection. IBA1+ cells were quantified in control (n = 61 fields) and metastatic tumour regions (n = 41 fields). Bar graph shows 1.95-fold increase of IBA1$^+$ cells in tumour compared with control tissue. P value was generated using a two-sided, unpaired t-test, and error bars show mean ± standard deviation. **d**, IF staining shows IBA1$^+$ cells (red) in normal human brain and three resected patient BCBM tumors. Insets show cell morphology, exhibiting evenly spaced, ramified microglia in normal human brain contrasting heavily infiltrated ameboid microglia in BCBM patients. Results are representative of a single experiment. Scale bar = 50 µm.

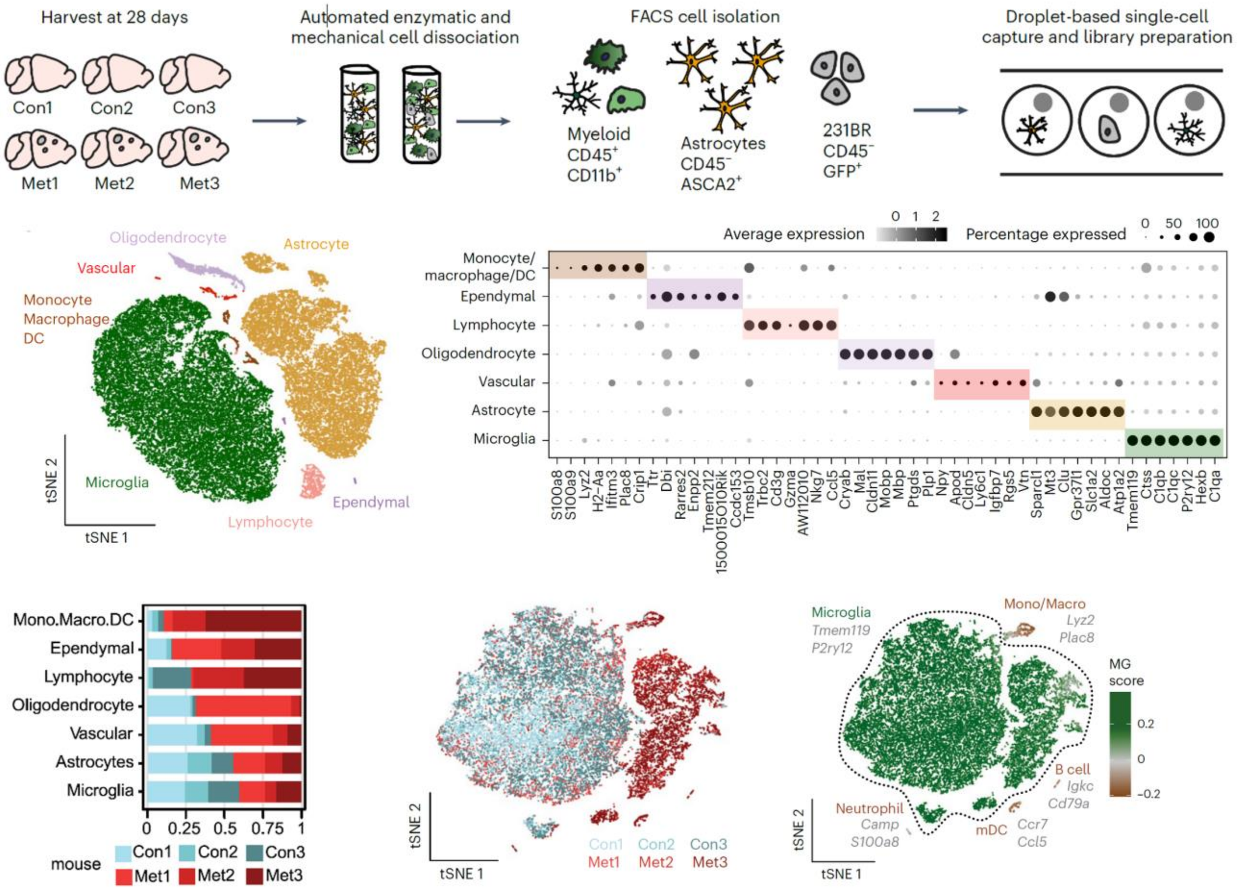

Figure 1.2 Single-cell analysis of TAMs in BCBM. a, Schematic showing experimental design for generation of scRNA-seq dataset. Foxn1$^{nu/nu}$ mice were injected with 500,000 GFP–Luc-labelled 231BR cells, and brains were collected 28 days later. Three metastatic (Met1–3) and three control (Con1–3)brains were digested and myeloid cells (CD45+, CD11b+), astrocytes (CD45−,ASCA2+) and 231BR (CD45−, GFP+) cells were isolated by flow cytometry fordroplet-based scRNA-seq. **b**, tSNE plot showing mouse cells that passed quality filtering (n = 42,891), coloured and labelled by cell type. **c**, Dot plot showing top marker genes for each cell type ranked by the average natural log fold change(FC) and determined by the Wilcoxon rank-sum test. Dot size represents the percentage of cells that express each gene, and dot greyscale represents the average expression level. For full marker gene list, see Supplementary Table 1. **d**, Bar chart shows the frequency of cells contributed by each mouse that localize to each cell type in Fig. 1.2b. **e**, tSNE plot showing clustering of myeloid cells (n = 24,348), coloured by mouse. **f**, tSNE plot showing each myeloid cell coloured by MG score, the core microglia gene signature from Bowman et al. (2016) that compared microglia with bone marrow-derived cells using bulk RNA-seq from lineage-labelled mice. For full MG score gene list, see Supplementary Table 3. Scores were calculated using the AddModuleScore function in Seurat. Top marker genes (grey) for each myeloid cell type were identified using the Wilcoxon rank-sum test. For myeloid cell type markers, see Supplementary Table 4. mDC, mature dendritic cell; Mono/Macro, monocytes and macrophages.

fold increase, p<0.0001)(Fig 1.1b, c). These data show that TAMs immediately interact with metastatic cells and accumulate within mouse and human BCBM.

We used scRNA-seq to interrogate the specific response of microglia to BCBM using the 231BR mouse model. Cells were dissociated from control (n=3) and metastatic brains (n=3) harvested at day 28 post 231BR injection, and CD45^{+}CD11b^{+} myeloid cells were isolated by flow cytometry (Fig 1.2a). ASCA2^{+} cells were sorted for control, and all cells were analyzed using droplet-based scRNA-seq technology (Chromium). Analysis of the 42,891 cells that passed quality control filtering (Fig 1.2b) revealed seven distinct cell types identified by lineage-specific markers (Fig 1.2c). This included the targeted cell types, astrocytes (*Aldoc, Atp1a2*), microglia (*Tmem119, P2ry12*) and non-microglia myeloid cells (*Lyz2, Plac8*) (Table S1). We also recovered small numbers of ependymal cells (*Ccdc153, Rarres2*), oligodendrocytes

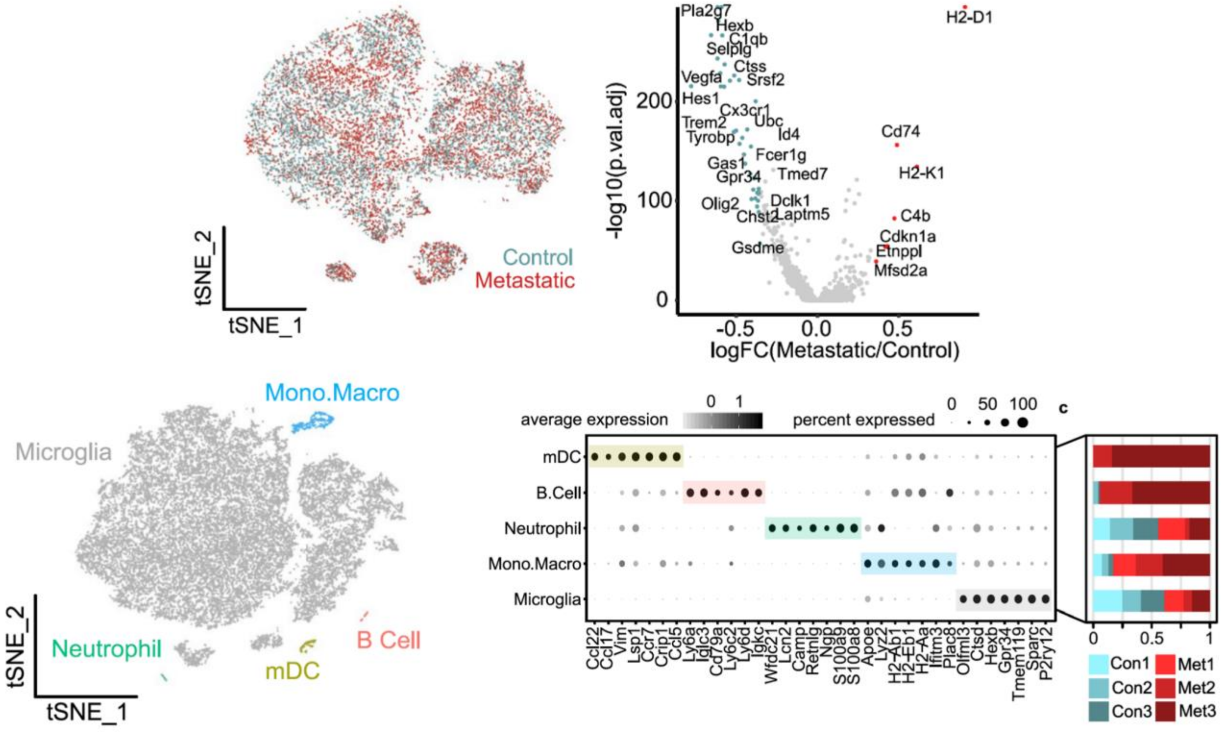

Figure 1.3. Single-cell analysis of alternative populations in BCBM. a, tSNE plot shows astrocytes colored by control or metastatic condition. **b**, Volcano plot shows genes differentially expressed (n = 6,542) between astrocytes from control and metastatic brains determined by Wilcoxon rank sum test, (p < 0.01). See Supplementary Table 2 for full list. Select genes with an absolute value average natural logFC >0.35 are colored and labeled. The y-axis represents the -log10 of Bonferroni corrected P values, and the x-axis represents average natural logFC between conditions. **c**, tSNE plot shows myeloid cells (n = 15,288) colored and labeled by cell type. mDC = mature dendritic cell. Mono.Macro = monocytes and macrophages. **d**, Dot plot shows top marker genes for each cell type ranked by average natural logFC. Dot size represents the percentage of cells that express the gene, and dot greyscale represents the average expression level. See Supplementary Table 4.

(*Mbp, Ptgds*), vascular cells (*Cldn5, Vtn*), and lymphocytes (*Cd3g, Gzma*). Lymphocytes and the non-microglia myeloid populations were preferentially from the metastatic condition, suggesting these cells are recruited from the periphery in response to tumor growth (Fig 1.2d). We found limited differences between astrocytes from control and metastatic brains and did not pursue further analysis of these cells (Fig 1.3a, b, Table S2).

Analysis of the 24,348 myeloid cells in the dataset revealed strong separation of control and metastatic conditions (Fig 1.2e). Microglia were distinguished from other myeloid populations by scoring each cell for the core microglia signature developed by Bowman et al (2016), which compared microglia to BMDMs using bulk RNA-seq from lineage labeled mice (Fig 1.2f, Table S3)[69]. Gene scoring identified two large microglia populations *(Tmem119, P2ry12, Sparc, Gpr34)*, where one contained microglia from both control and metastatic and the other was almost entirely from metastatic (Fig 1.2e). We also found two small populations of microglia that display an increased stress response, which is common post tissue manipulation[70]. Neutrophils (*Camp*, *S100a9*), monocytes/macrophages (*Ly6c2, Lyz2*), mature dendritic cells (*Ccr7, Flt3*), and B cells (*Igkc, Cd79a*) were also identified (Fig 1.3c, d, Table S4).

Further analysis of the microglia revealed robust changes in BCBM. We identified 3,715 genes differentially expressed between microglia from control and metastatic brains (adjusted $p<0.05$) (Table S4). Gene Ontology (GO) analysis of this BCBM response signature identified 'cytokine production,' 'antigen processing and presentation,' 'cellular response to IL-1,' 'response to IFN-gamma,' and 'response to IFN-beta' as top upregulated pathways, suggesting that microglia undergo a pro-inflammatory response to brain metastasis (Fig 1.4a)[71]. Further analysis revealed that these gene expression programs are not uniformly upregulated by all microglia. We used a probabilistic clustering method called latent dirichlet allocation (LDA), also known as topic modeling, to assess microglia heterogeneity (Fig 1.4b). Unlike standard cell clustering methods, topic modeling assigns each cell to

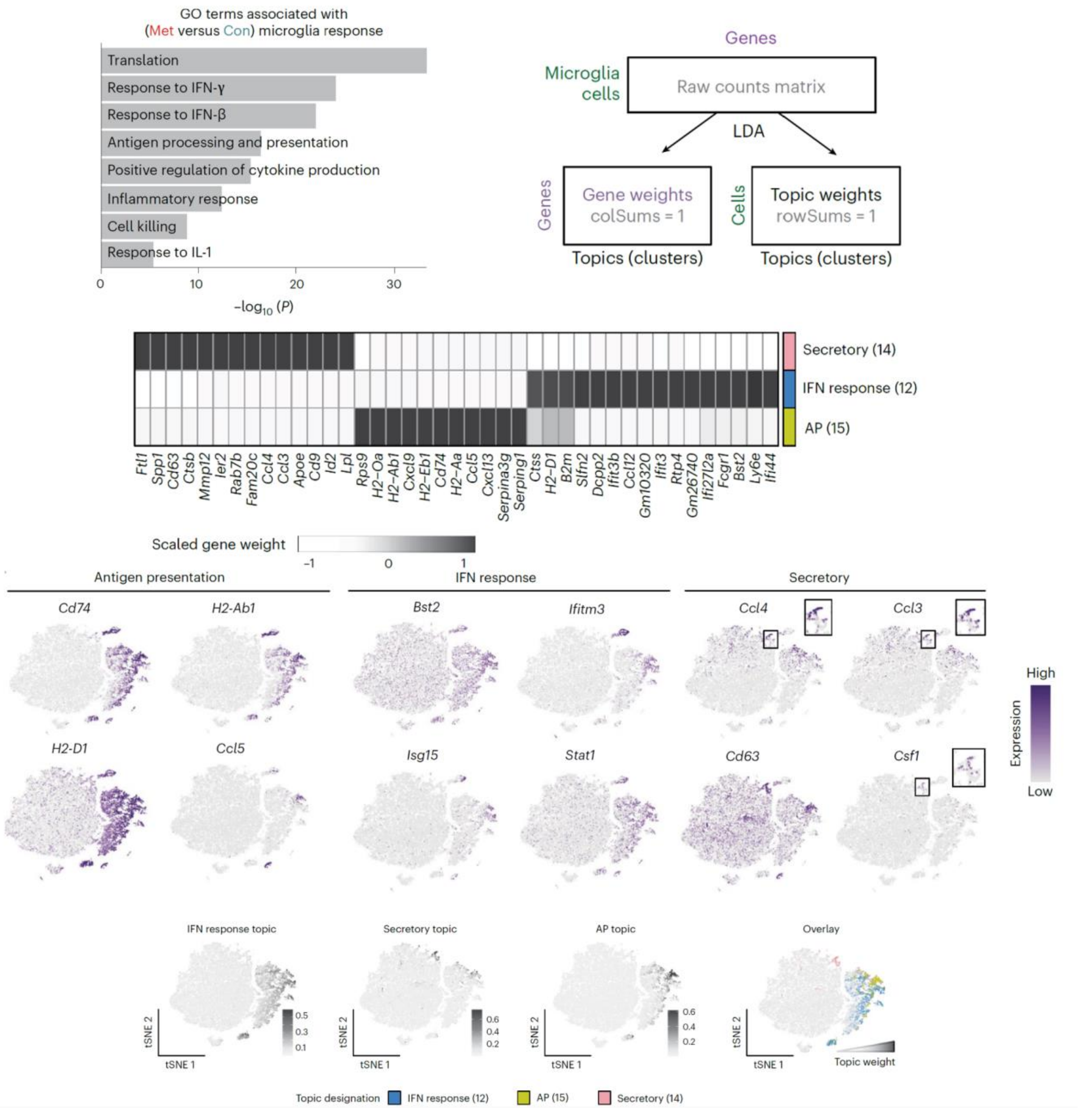

Figure 1.4 Microglia display a robust pro-inflammatory response to BCBM. a, Bar plot showing selected top GO terms associated with the BCBM response microglia signature. This signature was generated by differential gene expression analysis of microglia from metastatic versus control brains (n = 632 upregulated genes, adjusted P < 0.05). Differentially expressed (DE) genes were determined using the Wilcoxon rank sum test. GO terms were identified using MouseMine and select upregulated terms with Holm–Bonferroni-adjusted P values < 0.05 were retained. For DE genes, see Supplementary Table 4. **b**, Schematic overview of topic model fitting method to assess microglia heterogeneity. The CountClust R package was used to fit a topic model using LDA. A matrix for 'gene weights' was generated that contains a list of the genes comprising each topic and the gene weight (Supplementary Table 5). A second matrix for 'topic weights' lists the weight of each topic across the cells. **c**, Heatmap showing three core topics upregulated in microglia in BCBM. Scaled gene weights for top genes comprising each topic are shown. **d**, tSNE plots showing expression of selected genes from each topic in myeloid cells. **e**, tSNE plots showing distribution of three core topics in each microglia. Left panels show topic weight in each cell indicated by contrast greyscale. Right panel overlay shows top topic assignment for each cell, where only cells with a topic weight >0.1 are coloured.

multiple gene modules or topics, which allows for better appreciation of how distinct but overlapping gene modules are expressed in a population of cells[72].This analysis identified four topics that had a higher average weight in all three mice with BCBM compared to controls. Topic 12 was the most broadly upregulated and represented an interferon (IFN) response program (*Bst2, Ifitm3, Ifit3b, Isg15*) similar to reports in other disease contexts, including Alzheimer's disease (AD)[73], aging[74], injury[74] and glioma[75] (Fig 1.4c-e). IFN response genes are upregulated in response to disease and induce effector function in immune cells[76]. In microglia, the IFN response program may represent their initial sensing of metastatic infiltration and tissue damage. Topic 15 showed a more restricted expression pattern and was enriched for genes associated with antigen presentation (AP) (*Cd74, H2-Aa, H2-D1*) (Fig 1.4c-e), which has also been observed in glioma and AD[73,75]. AP genes enable antigen presentation to T cells, raising the question of whether microglia present antigen locally to T cells in the CNS to maintain their activation.

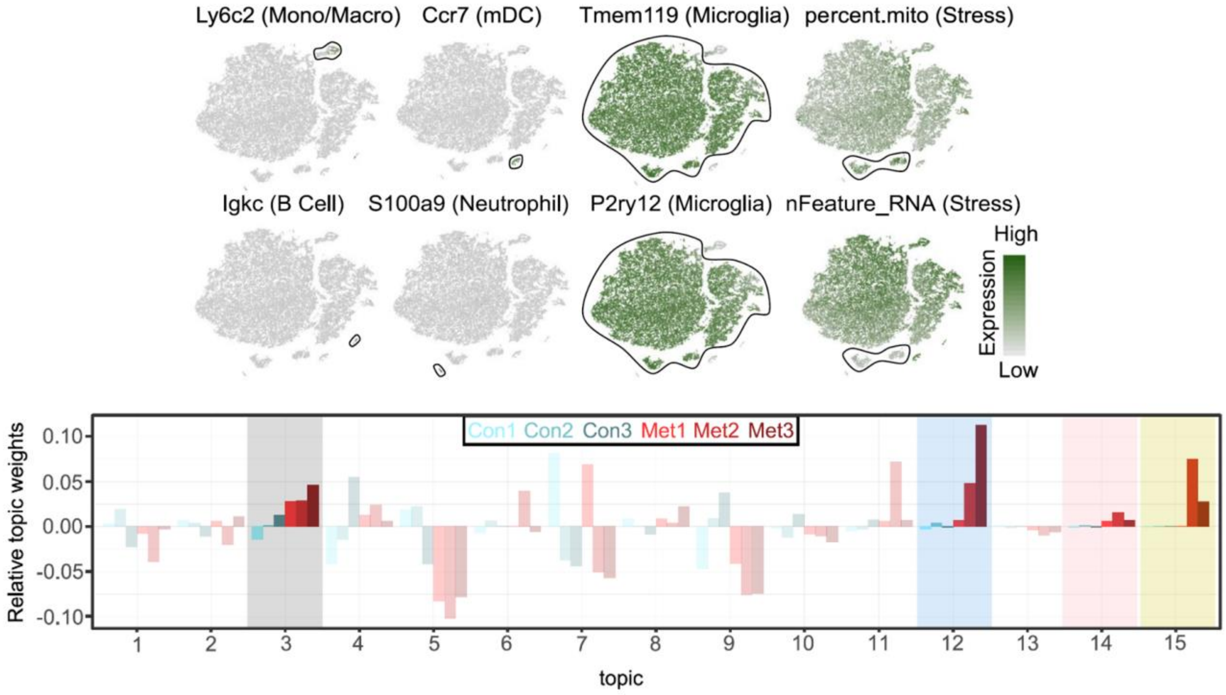

Figure1.5 a, **Subcluster analysis of proinflammatory microglia.** Feature plots show myeloid cells colored by canonical cell type marker genes or features. Stressed cells were identified by increased expression of mitochondrial genome (percent.mito) genes, and decreased number of genes detected (nFeature_RNA). **b**, Bar plot shows the relative enrichment of each topic in control and metastatic animals from Fig. 2d. The relative enrichment was determined by subtracting the average topic assignment for the control mice from the average topic assignment across all cells in each mouse. Highlighted topics show four core topics where all three metastatic mice have a higher relative enrichment than all three control mice (that is min(Metastatic) > max(Control)).

Topic 14 was associated with a secretory phenotype and was also expressed by a small subset of microglia (Fig 1.4c-e). This topic was enriched for genes associated with exosomes (*Cd63*), lipid metabolism (*Apoe, Lpl*), and cytokines (*Spp1, Csf1, Il1b, Tnf)* (Fig 1.4c,e). This topic strongly overlaps with the signature of disease associated microglia or "DAMs", a population of phagocytic microglia identified in mouse models of neurodegeneration[77]. The IFN response and AP topics both included genes encoding numerous chemokines for immune cell trafficking, including *Ccl2* and *Ccl12* (inflammatory monocytes), *Ccl3*, *Ccl4* and *Ccl5* (macrophage and NK cells), and *Cxcl9* and *Cxcl10* (CD8 T cells) (Fig 1.4c,e, Table S5). A final topic (topic 3) was enriched for ribosomal genes (*Eef1a1, Rps29, Rpl37*) (Fig 1.5a, b, Table S5), which could indicate cells with increased transcriptional capacity or stress response. Taken together, these data show that microglia upregulate multiple pro-inflammatory programs, suggesting they may play diverse roles in the immune response to BCBM.

We investigated the microglia pro-inflammatory response at the protein level in multiple different models of BCBM. We evaluated the expression of three key markers by flow cytometry: bone marrow stromal antigen 2 (BST2), major histocompatibility complex II (MHC-II) and CD74[78-81].

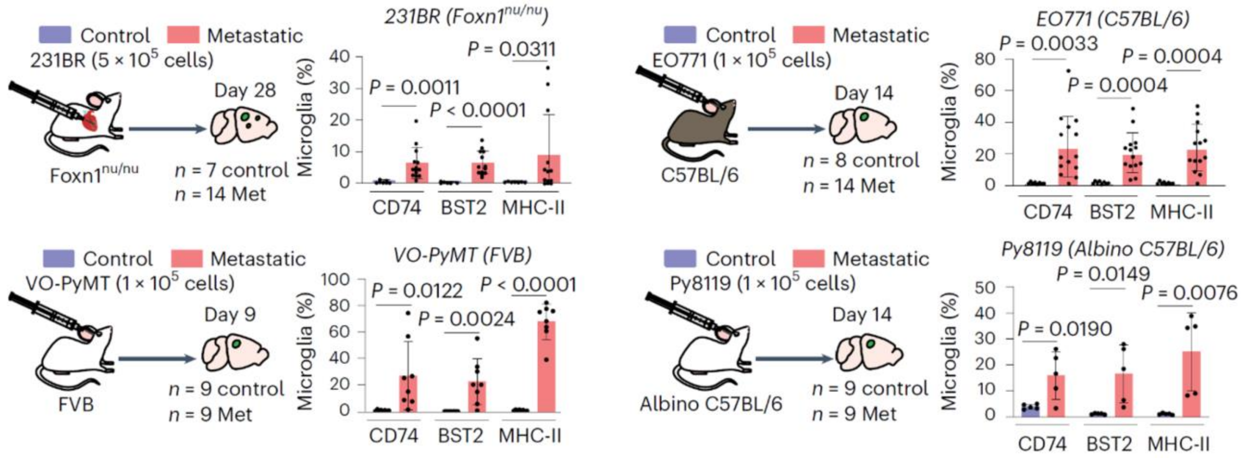

Figure 1.6 The Microglia pro-inflammatory response is conserved in diverse models of BCBM. Flow cytometry analysis of CD74, BST2 and MHC-II expression in microglia from four BCBM models. Microglia were identified by gating on CD45lo, CD11b+, Ly6C−cells[82,83]. Bar graphs show the percentage of microglia expressing each marker. P values were generated by an unpaired two-sided Student's t-test, error bars indicate mean ± standard deviation.

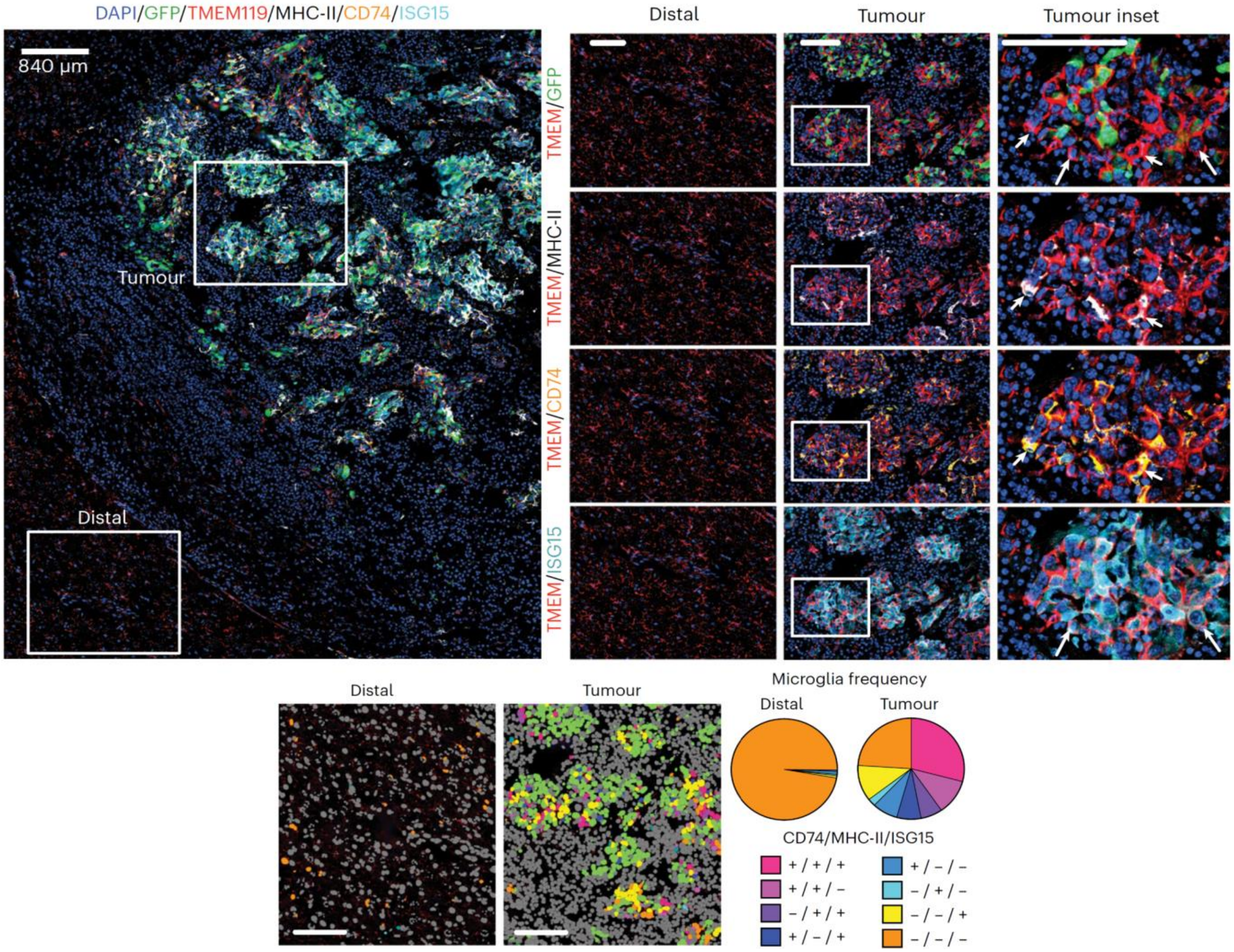

Figure 1.7 Spatial immunopheotyping isolates the inflammatory response to tumor-proximal parenchyma. a, In situ analysis of microglia proinflammatory marker expression by multiplex IF (CODEX). Brain tissue slices from mice bearing EO771–GFP tumours were stained for DAPI (blue), and antibodies against GFP (green), TMEM119 (red), MHC-II (white), CD74 (yellow) and ISG15 (cyan). Left: overview of all markers. Scale bar, 840 µm. Right: pairwise marker expression in higher-magnification insets of tumour and distal regions. Short arrows indicate representative microglia expressing AP markers (TMEM119+ MHC-II+CD74+), and long arrows indicate representative microglia expressing IFN response marker (TMEM119+ISG15+). Results are representative of two independent experiments. Scale bar, 100 µm. **b**, Quantification of pro-inflammatory markers in brain tissue slices. Microglia were identified on the basis of TMEM119 expression and then scored for marker expression. Left: images showing phenotype in representative tumour and distal regions. Tumour cells (ISG15+TMEM119−) and other non-microglia cells (TMEM119−CD74−MHC-II−ISG15−) are shown in green and grey, respectively. Right: pie graphs showing the proportion of microglia displaying marker combinations. Frequencies are as follows: CD74+MHCII+ISG15+, distal <0.01, tumour 0.29; CD74+MHC-II+ISG15−, distal <0.01, tumour 0.11; CD74−MHC-II+ISG15+, distal <0.01, tumour 0.07; CD74+MHC-II−ISG15+, distal <0.01, tumour 0.07; CD74+MHC-II−ISG15− distal 0.01, tumour 0.08; CD74−MHC-II+ISG15−, distal <0.01, tumour 0.02; CD74−MHC-II−ISG15+, distal 0.01, tumour 0.11; CD74−MHC-II−ISG15, distal 0.97, tumour 0.24. n = 4 mice per condition. Scale bar, 100 µm.

Brain tissues were harvested at endpoint and microglia were identified by gating on $CD45^{lo}CD11b^{+}Ly6C^{-}$ cells[82,83]. Remarkably, we observed a consistent increase of marker expression in each model (Fig 1.6), validating our findings by scRNA-seq.

We evaluated the spatial localization of key markers in the EO771-C57BL/6 model by multiplex IF (co-detection by indexing, CODEX). We co-stained for MHC-II, CD74, and IFN stimulated gene 15 (ISG15), as well as TMEM119 and GFP to identify microglia and tumor cells, respectively. This analysis showed that pro-inflammatory microglia specifically localize proximal to tumor cells, while distal microglia remain negative (Fig 1.7a, b). In tumor regions, we found that the highest frequency of microglia co-expressed all three markers (MHC-II$^+$CD74$^+$ISG15$^+$, 29%) (Fig 1.7b). The next most abundant were homeostatic microglia that expressed none of the markers (MHC-II$^-$CD74$^-$ISG15$^-$, 24%), followed by microglia that express only the AP markers (MHC-II$^+$CD74$^+$ISG15$^-$, 11%) and microglia that expressed only the IFN response marker (MHCIICD74$^-$ISG15$^+$, 11%) (Fig 1.7b). Only rare microglia with other combinations were identified. These data are consistent with our topic modeling, and show substantial marker overlap but notable exclusivity of the AP and IFN response programs into subsets of microglia.

We further investigated the pro-inflammatory function of microglia using a cytokine array (Eve technologies). We compared cytokine expression in microglia from control and EO771 tumor-bearing brains. We observed upregulation of several cytokines consistent with our scRNAseq analysis, including macrophage colony-stimulating factor (CSF1), chemokine ligand 5 (CCL5), chemokine ligand 9 (CXCL9) and chemokine ligand 10 (CXCL10) (Fig 1.8)[85,86]. Taken together, these data validate our scRNA-seq results at the protein level and demonstrate that microglia display a pro-inflammatory response to BCBM.

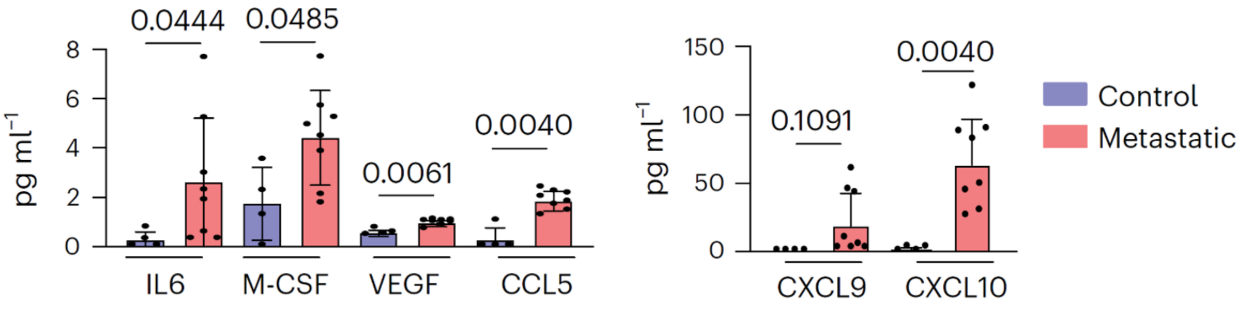

Figure 1.8 Analysis of cytokine expression by microglia in BCBM. Microglia were isolated from control (n = 4) and metastatic (EO771-C57BL/6, n = 8) brains by flow cytometry, and cell lysates were analysed by cytokine array (Eve Technologies). P values shown are the result of a two-sided unpaired Mann–Whitney t-test.

Microglia suppress tumor growth through recruitment and activation of lymphocytes

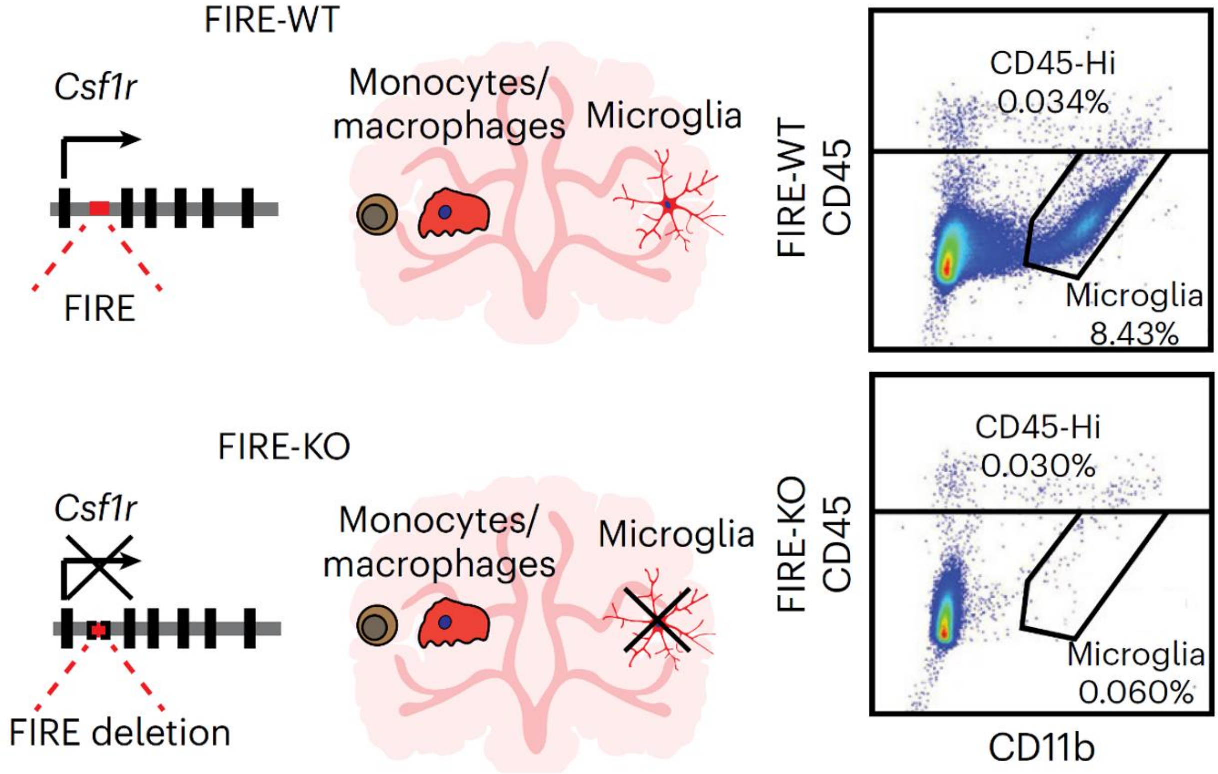

Figure 2.1 The FIRE model for germline depletion of microglia. a, Schematic depiction of Csf1r$^{\Delta FIRE/\Delta FIRE}$ mouse model. Deletion of FIRE super-enhancer in FIRE-KO mice leads to loss of CSF1R protein expression in yolk-sac derived macrophages. In the CNS, microglia do not develop, while monocyte and macrophage numbers are unaffected. **b**, Representative flow cytometry plots show the percentage of CD45loCD11b+ microglia and CD45hi immune cells gated from live (Sytox negative), single cells in FIRE-WT (n = 2) and FIRE-KO (n = 2) mouse brains.

Prior work using pharmacologic and genetic depletion strategies has established a clear pro-tumorigenic role for TAMs in BCBM and CNS cancers[19–22]. These studies primarily utilized CSF1R inhibitors and CX3CR1-targeted genetic ablation strategies that can target microglia as well as other TAM populations, leaving the specific role of microglia unclear[20,22,88,89]. A genetic model was recently developed that completely lacks microglia due to deletion of the highly conserved super-enhancer in the *Csf1r* locus called the fms-intronic regulatory element (FIRE) (Fig 2.1)[24]. The *Csf1r*$^{\Delta FIRE/\Delta FIRE}$ (FIRE-KO) model lacks microglia while retaining most BAMs and BMDMs, which we confirmed by flow cytometry, making it an important tool to specifically explore microglia function in disease[24,90].

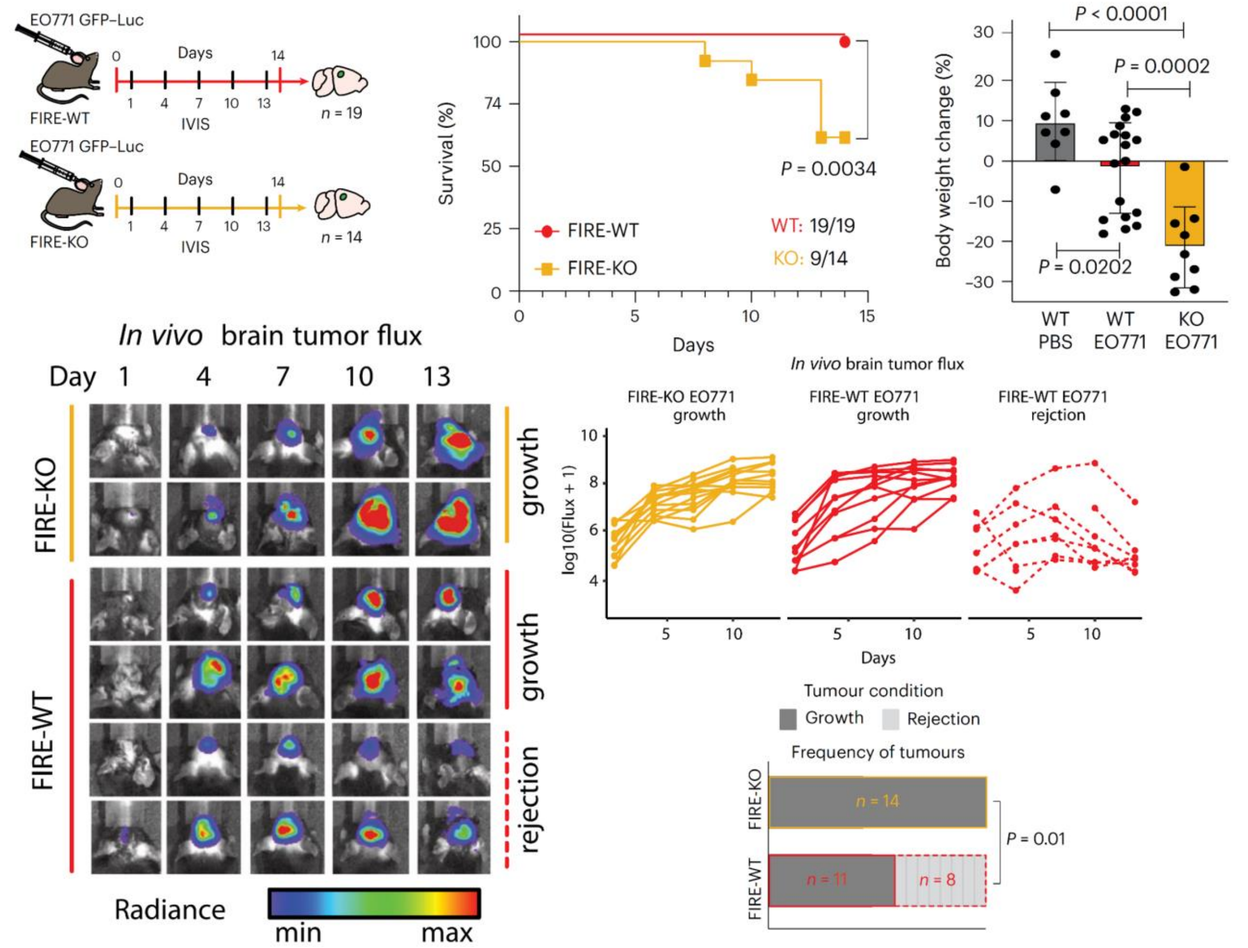

Figure 2.2 Genetic ablation of microglia reduces capacity for tumor rejection. a, Schematic of experimental design to compare disease progression in FIRE-WT and FIRE-KO mice. FIRE-WT (n = 19) and FIRE-KO (n = 14) mice were injected intracranially with 100,000 GFP- and luciferase (GFP–Luc)- labelled EO771 cells. Control FIRE-WT mice (n = 8) were also injected with PBS. Animals were imaged for luminescence (IVIS) every 3 days before dissection at endpoint on day 14. **b**, Kaplan–Meier plot shows survival in FIRE-WT (19/19, 100%) and FIRE-KO (9/14, 64%) mice. P value determined by log-rank (Mantel–Cox) test. **c**, Bar graph shows percentage body weight change for surviving PBS-injected (n = 8), FIRE-WT (n = 19) and FIRE-KO (n = 9) animal from d at day 14 relative to day 0. P values determined by unpaired two-sided Student's t-test, and error bars represent mean ± standard deviation. **d**, IVIS images show EO771 luciferase luminescence signal change over time in FIRE-WT and FIRE-KO animals. Representative animals that displayed continuous signal increase (tumor growth, solid line) vs. signal decrease (tumor rejection, dashed line) are shown. Pseudocoloring of luminescence shows quantification of radiance (p/sec/cm2/sr). **e**, Line graphs show quantification of luminescence signal change over time in all FIRE-WT and FIRE-KO animals. Solid lines indicate animals that demonstrated tumor growth and dashed lines indicate those that showed tumor rejection. Growth was defined by signal increase over time, and rejection was defined as either baseline signal (<106) or >5-fold decrease in signal relative to maximum. **f**, Bar graph summarizing the frequency of animals that displayed tumour growth and tumour rejection in FIRE-WT and FIRE-KO mice. Tumour rejection was defined by a lack of engraftment or engraftment followed by tumour rejection. P value was determined by two-sided Fisher's exact test.

We investigated the role of microglia in BCBM by comparing tumor progression in FIRE-WT and FIRE-KO animals. FIRE-WT (n=19) and FIRE-KO (n=14) mice were injected with GFP and luciferase-labeled EO771 cells and monitored by *in vivo* bioluminescence (IVIS) every three days until endpoint at day 14 (Fig 2.2a). Surprisingly, many FIRE-KO mice quickly developed overt clinical symptoms of advanced disease (Fig 2.2b, c). Five of 14 FIRE-KO mice died before endpoint (36% mortality), while all 19 FIRE-WT survived (0% mortality) (p=0.0034) (Fig 2.2b). Surviving FIRE-KO mice displayed >20% decrease in body mass compared to FIRE-WT (p=0.0002), also indicating increased morbidity in mice lacking microglia (Fig 2.2c). Analysis of tumor growth over time by IVIS revealed interesting differences in the kinetics of tumor progression between FIREWT and FIRE-KO animals (Fig 2.2d-f). We observed tumor rejection (defined by lack of engraftment, or engraftment followed by tumor regression) in eight of 19 FIRE-WT mice over time, while signal continued to increase in all 14 FIRE-KO animals (p=0.01) (Fig 2.2f). We further compared tumor engraftment in FIRE-KO and FIRE-WT mice using a serial dilution approach, where we injected animals with 10 – 200 x 10^4 E0771 cells. This showed increased engraftment efficiency and larger tumor growth in FIRE-KO compared to FIRE-WT mice at each dilution. Together, these data show that animals lacking microglia demonstrate increased tumor progression and decreased capacity for tumor rejection.

We hypothesized that microglia promote tumor rejection by promoting an anti-tumor T cell response in the CNS. We tested this hypothesis using the FIRE-KO model to determine whether animals lacking microglia show a reduced T cell response to BCBM. We injected EO771 cells into FIRE-WT (n=8) and FIRE-KO (n=8) animals and compared the immune response in the brain on day 7 (Fig 2.3a). We chose this time point because it is when we begin to observe tumor rejection. Ex vivo analysis showed no significant difference in tumor size at this timepoint (Fig 2.3b). We quantified the number and frequency of NK, T, and myeloid cell populations by flow cytometry. Consistent with our hypothesis, FIRE-KO mice had reduced numbers and frequencies of all T cell subsets, including CD4$^+$, CD8$^+$ and T

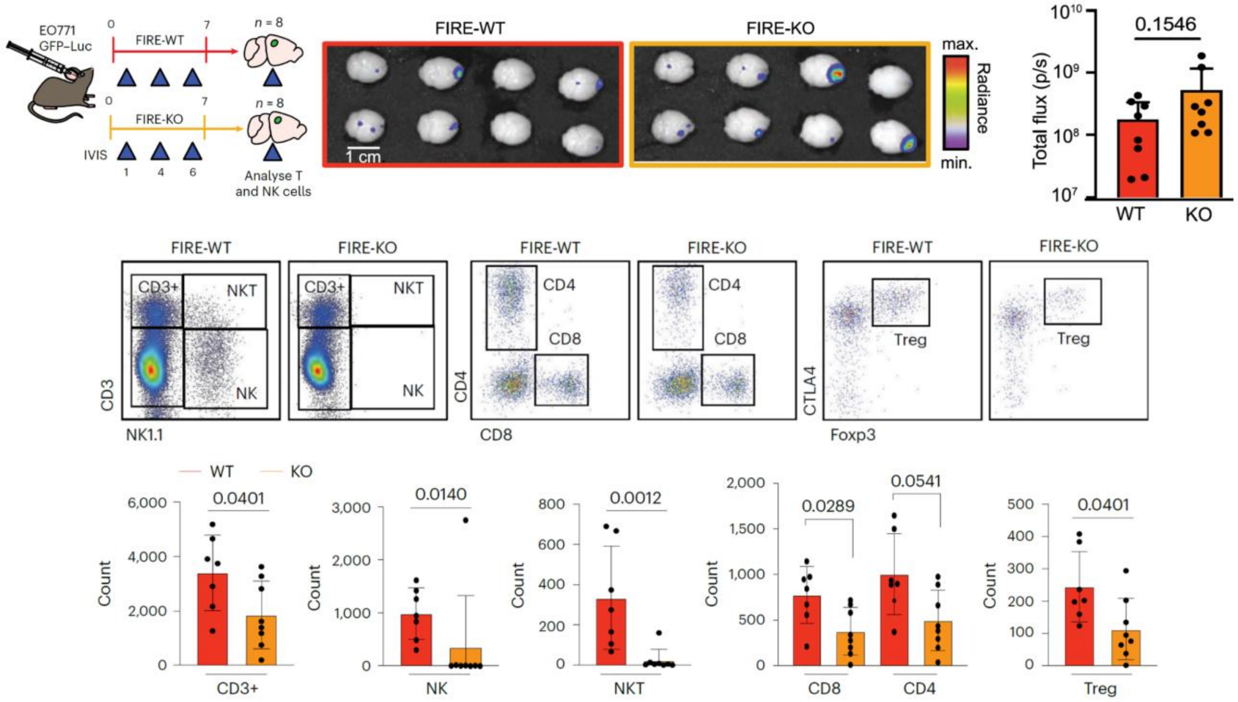

Figure 2.3 Microglia promote the lymphocyte response to BCBM. a, Schematic of experimental design to compare NK and T cell responses in FIRE-WT and FIRE-KO EO771 tumour-bearing mice. FIRE-WT (n = 8) and FIRE-KO (n = 8) mice were injected intracranially with 100,000 EO771 GFP–Luc cells. Animals were imaged for luminescence (IVIS) on days 1, 4 and 6 before dissection on day 7. **b**, Quantification of tumor burden in FIRE-WT and FIRE-KO animals (n = 8/group). Mice were injected with EO771 GFP-Luc cells as described in Fig. 5a and tumors were harvested and analyzed by IVIS on day 7. Images (left panels) show pseudocoloring of radiance (p/sec/cm2/sr), and bar graph shows quantification of total flux (p/s). P value shown is the result of a student's unpaired two sided t-test. Error bars represent mean +/− standard deviation. **c**, Analysis of NK and T cell subsets in FIRE-WT (n = 7) and FIRE-KO (n = 8) mice by flow cytometry. Representative FACS plots show gating for each NK and T cell subset after gating for single, live (Sytox-negative) cells. **d**, Bar graphs showing cell counts for NK and T cell subsets. Counts shown are out of 100,000 single, live cells analysed. P values are the result of a Student's unpaired two-sided t-test. Error bars represent mean ± standard deviation

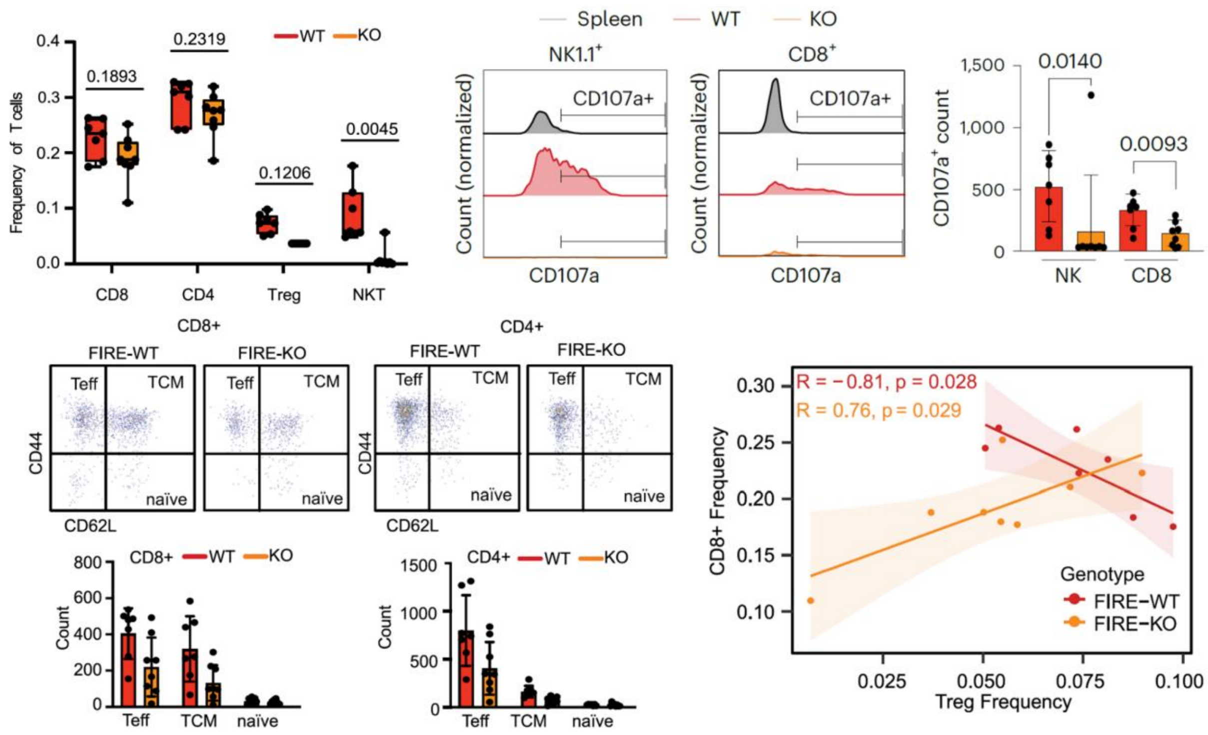

Figure 2.4 Analysis of NK, T, and monocyte responses to BCBM in FIRE-WT and FIRE-KO animals. a, Box plots show frequency of T cell subsets from Fig. 2.3d (n = 7 FIRE-WT, n = 8 FIRE-KO). Frequencies shown are out of all T cells. Bounds of box and whiskers are indicative of the first through fourth interquartile range. P value shown is the result of a student's un-paired two sided t-test. **b**, Analysis of CD107a expression in NK and CD8+ T cells by flow cytometry. FACS plots (left) show expression of CD107a from spleen and brains of representative animals from each cohort. Bar graph shows cell counts out of 100,000 single, live cells. P values are the result of a Student's unpaired two-sided t-test. Error bars represent mean ± standard deviation. **c**, Analysis of T cell activation in tumor bearing FIRE-WT and FIRE-KO brain tissues by flow cytometry. CD44 and CD62L expressions were measured in CD4 and CD8 T cells to delineate T effector (Teff), T central memory (TCM) and naive T cell subsets. Representative FACS plots (top panels) show gating for each subset after gating for single, live (Sytox negative) cells. Bar graphs (bottom panels) show quantification of T cell counts for each group. Error bars represent mean +/− standard deviation. Pairwise comparisons of counts between groups were not significant. **d**, Linear regression model of CD8+ T cell and Treg quantification from Fig 2.5a. R-squared and P values determined by simple linear regression function.

regulatory (Treg) cells (Fig 2.3c, d). Remarkably, NK and NKT cells were almost completely absent in FIRE-KO animals (Fig 2.3d).

Further analysis of effector, central memory and effector function status by CD44, CD62L and CD107a expression showed consistent reductions in the numbers of CD8$^+$ and CD4$^+$ effectors and central memory T cells in FIRE-KO (Fig 2.4a, c). We also found a significant decrease in the number of degranulating CD107a$^+$ NK and CD8$^+$ cells in FIRE-KO (Fig 2.4b). We also looked for correlations between T cell subset frequencies and found that the CD8$^+$ T cell frequency negatively correlates with Tregs in FIRE-WT (R= -0.81, p= 0.028), but positively in FIRE-KO (R=0.76, p= 0.029) (Fig 2.4d). This means that in FIRE-WT, mice with more CD8$^+$ T cells have fewer Tregs, while in FIRE-KO, mice with more CD8$^+$ T cells also have more Tregs. Thus, in the absence of microglia, the CD8$^+$ T cells may be less effective at inducing tumor rejection because there are relatively more immunosuppressive Tregs. Analysis of CD11b$^+$Ly6c$^+$ monocytes showed no significant difference in their numbers between FIRE-WT and FIRE-KO (Fig 2.5). In sum, these data suggest that microglia promote an anti-tumor immune microenvironment through supporting NK, NKT, and T cell responses to BCBM.

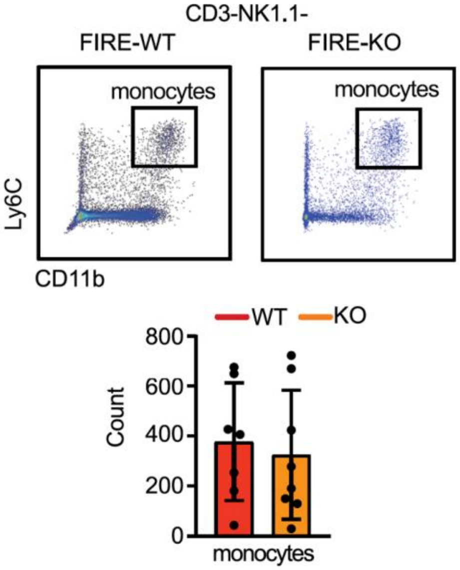

Figure 2.5 Quantification of monocytes in tumor bearing FIRE-WT and FIRE-KO brain tissues by flow cytometry. CD11b+Ly6C+ monocytes were identified following gating for CD3−NK1.1−, single, live (Sytox negative) cells. Top panels show representative FACS plots, and bottom panels show quantification of cell counts. Error bars represent mean +/− standard deviation. Pairwise comparisons of counts between groups were not significant.

Microglia – T cell reciprocity coordinates the anti-tumor immune response

We further investigated whether the tumor suppressive effect of microglia is mediated through T cells. We tested whether we could abolish the tumor suppressive effect of microglia in FIRE WT animals by inhibiting T cell trafficking to the CNS with S1P inhibitors (FTY720), or using RAG1 KO mice that lack T cells. We generated three cohorts of animals, RAG1-KO (n=12), FTY720 treated (n=6), and vehicle treated (n=13) (Fig 3.1a). All animals were injected with EO771 cells on day 0. FTY720 and vehicle were injected daily starting on day 0 until endpoint on day 12. Flow cytometry analysis confirmed T cell depletion in the brain, showing a 5.2-fold reduction in FTY720 treated mice ($p<0.0001$) and a complete absence in RAG1-KO (Fig 3.1b). The frequencies of microglia and monocytes were not significantly different among the groups.

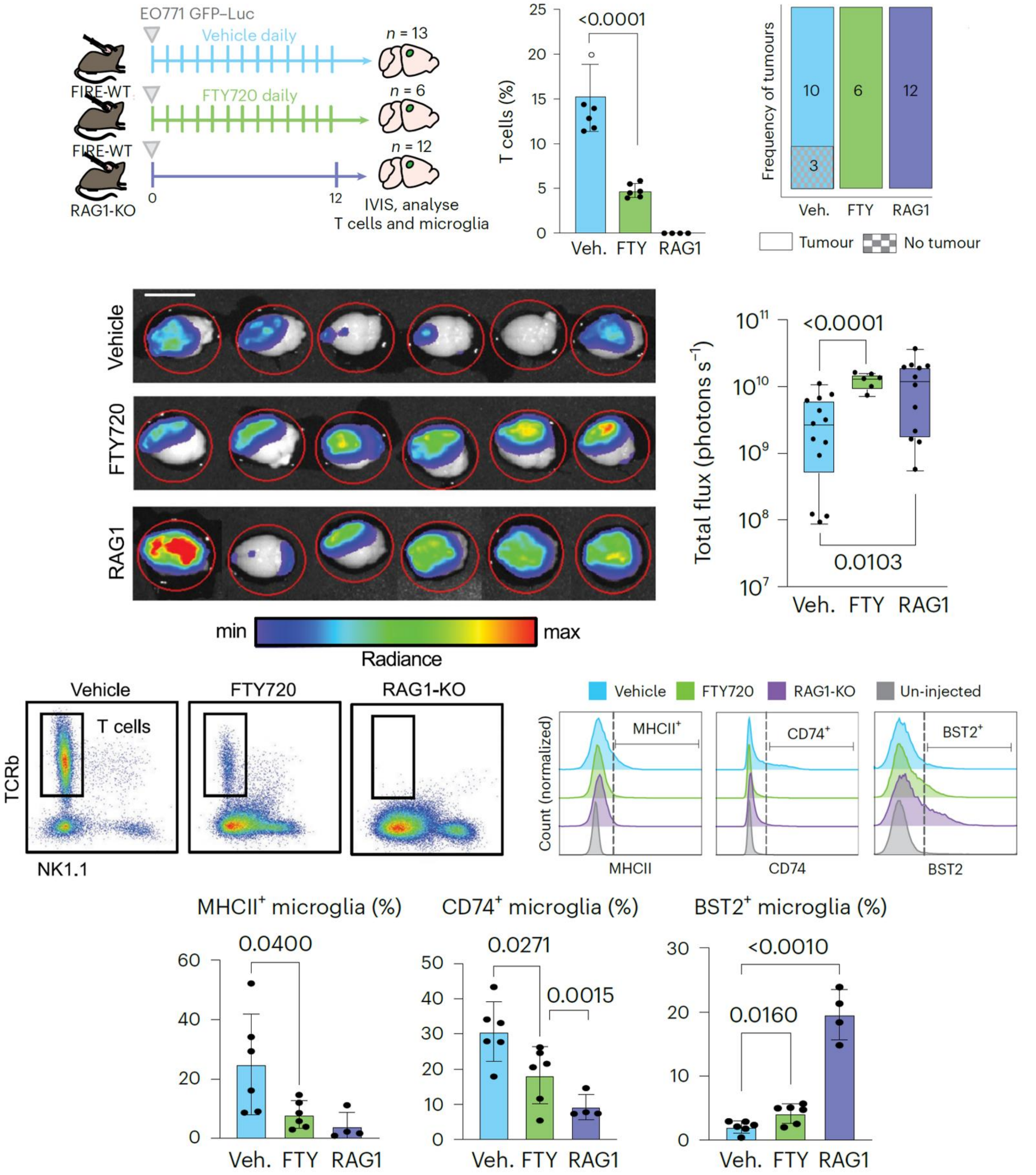

Figure 3.1 (cont, p21) T cell infiltration enhances the microglial antitumor response. a, Schematic of experimental design to determine effects of T cell deficiency on BCBM. Tumour burden was compared in three cohorts of animals, FIRE-WT vehicle treated (Veh., n = 13), FIRE-WT FTY720 treated (FTY, n = 6) and RAG1-KO (RAG1, n = 12). Vehicle (PBS + 0.1% DMSO) or FTY720 (5 mg kg−1) were administered via intraperitoneal injection to FIRE-WT animals on day 0 and repeated daily. A total of 70,000 EO771 GFP–Luc cells were delivered to each animal in all three cohorts by intracranial injection on day 0 following drug delivery. Brain tissues were collected at endpoint on day 12 and analysed for tumour burden by IVIS and immune response by flow cytometry. b, Bar graph showing the percentage of TCRb+ T cells in brain tissues collected from each cohort (n = 6 Veh., n = 6 FTY, n = 4 RAG1) of animals at endpoint, gated out of single, live (Sytox negative) CD45hi cells as shown in Fig. 3.1e. P values shown are the result of an unpaired two-sided Student's t-test. Error bars represent mean ± standard deviation. **c**, Quantification of EO771 tumour engraftment at endpoint on day 12 by IVIS. Bar graph shows frequency of animals in vehicle (Veh.), FTY720 (FTY) and RAG1-KO (RAG1) groups that grew tumours. P = 0.51 Veh. versus FTY. and P = 0.21 Veh versus RAG1 by two-sided Fisher's exact test (continues on p27).

Figure 3.1 (p26, cont) T cell infiltration enhances the microglial antitumor response. d, Quantification of EO771 tumour burden at endpoint on day 12 by IVIS. Pseudocolor shows radiance (p/sec/cm2/sr) in each whole brain. Box-and-whisker plots show total flux per brain of vehicle (Veh.)- and FTY720 (FTY)-injected FIRE-WT and RAG1-KO (RAG1) cohorts. Bounds of box and whiskers are indicative of the first through fourth interquartile range. P values shown are the result of an unpaired two-sided Student's t-test. **e**, Gating scheme for analysis of T cells in brain tissue harvested from vehicle treated, FTY720 treated and RAG1-KO mice. FACS plots show gating of TCRb+ T cells from single, live (sytox negative) CD45hiCD11b− cells from Fig. 3.1a. **f**, Analysis of pro-inflammatory marker expression in microglia from T cell-deficient mice (n = 6 Veh., n = 6 FTY, n = 4 RAG1). histograms showing expression of MHC-II, CD74 and BST2 in representative animals, following gating on single, live (Sytox negative) CD45intCD11b+Ly6c-. **g**, Bar graphs showing the percentage of marker positive microglia in each cohort. P values are the result of an unpaired two-sided Student's t-test. Error bars represent mean ± standard deviation.

In both FTY720 and RAG1-KO groups, we found increased tumor engraftment and tumor burden ($p<0.0001$, and $p=0.0103$) relative to control animals (Fig 3.1c, d)**.** This shows that microglia replete animals are less able to suppress BCBM in the absence of T cells, suggesting that microglia suppress BCBM in part through supporting the T cell response.

We also found interesting differences in microglia marker expression between wildtype and T cell deficient animals. Microglia from FTY720 treated mice showed 3.1- and 1.6-fold lower percentages of the AP markers MHC-II+ ($p=0.0400$) and CD74+ ($p=0.0271$), respectively (Fig 3.1f, g). The reduced expression of these proteins was even more pronounced in RAG1-KO mice (Fig 3.1g), indicating that this is not simply an effect of FTY720 treatment, but rather due to the reduction or absence of T cells.

Furthermore, FTY720 treated and RAG1-KO mice had a 2-fold ($p=0.0160$) and 9.4-fold ($p<0.0001$) higher percentage of microglia positive for the IFN response protein BST2, respectively (Fig 3.1g). This suggests that T cells may be required to fully license microglia to upregulate the AP program, and without T cells, microglia are limited to the IFN response program.

We further tested this hypothesis using scRNA-seq to determine whether microglia upregulation of the AP program is dependent upon T cell infiltration. We transplanted EO771 cells into C57BL/6 (n=6) and RAG1-KO (n=6) mice and evaluated gene expression in sorted immune (CD45^{hi-int}) cells 4 and 10 days later (n=3 per group per time point) (Fig 3.2a). Clustering and marker gene analysis of the 31,053 cells that passed filtering identified nine major immune cell types (Fig 3.2b, c). We observed a 2-6-fold increase in the frequency of T cells from days 4 to 10, indicating increasing T cell infiltration with tumor progression. As expected, no T cells were detected from RAG1 KO mice (Fig3.2c). Subset analysis of the 1949 T cells showed a robust expansion of the T cell repertoire from day 4 to 10 (Fig 3.4 a). Most notable was the decrease in naïve T cells and increase in proliferating and CD8 effector T cells, showing that the relative frequency of activated T cells increases in the brain over time (Fig 3.4c).

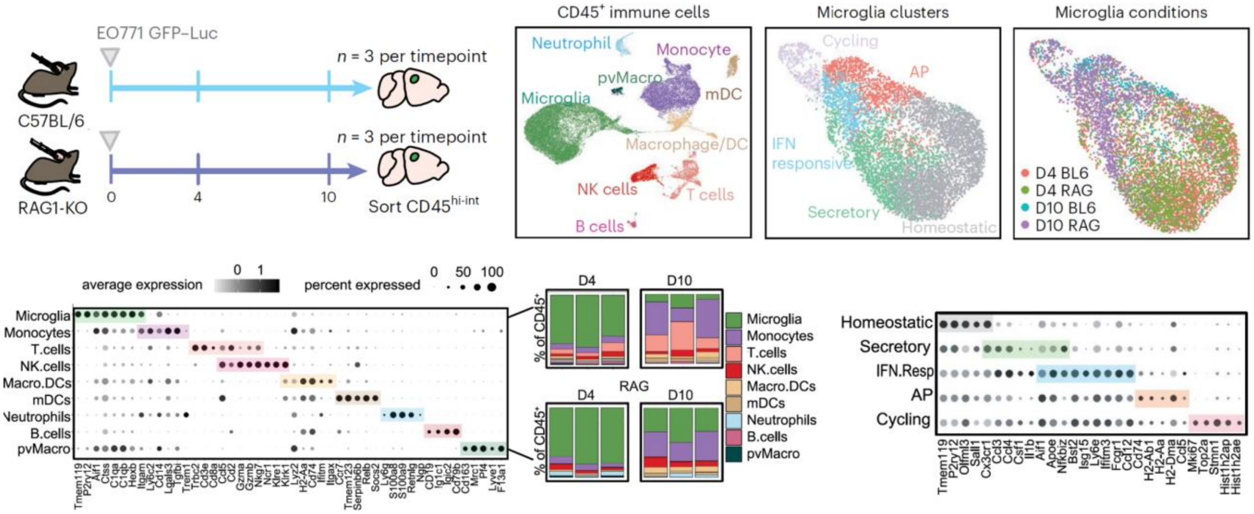

Figure 3.2 Clustering of BCBM infiltrating leukocytes in T cell replete and deficient mice. a, Schematic of experimental design to evaluate changes in microglia and T cell activation over time. A total of 100,000 EO771 GFP–Luc cells were administered through intracranial injection to C57BL/6 (n = 6) and RAG1-KO (n = 6) mice at day 0. Brain tissues were collected 4 days (n = 3 per group) and 10 days (n = 3 per group) post injection and sorted for live, CD45hi-int cells by flow cytometry for scRNA-seq analysis. **b**, UMAPs showing all immune cells (n = 31,053 cells) (left), microglia coloured by subcluster (middle) and microglia coloured by condition (right). UMAPs for microglia were downsampled to display an equal number of microglia from each condition (n = 1,000 cells per condition). **c**, Dot plot shows top marker genes for each cell type in total CD45hi-int sorted cells, ranked by the average log2 fold-change and determined by the Wilcoxon rank sum test. Dot size represents the percentage of cells that express each gene, and dot greyscale represents the average expression level. Macro.DCs = macrophages and dendritic cells, mDCs = mature dendritic cells, pvMacro = perivascular macrophages. Bar graphs illustrate relative contribution of each cluster to total leukocytes, separated by mouse strain and timepoint. **d**, Dot plot shows expression of top marker genes for each microglia cell cluster from Fig. 3.2b.

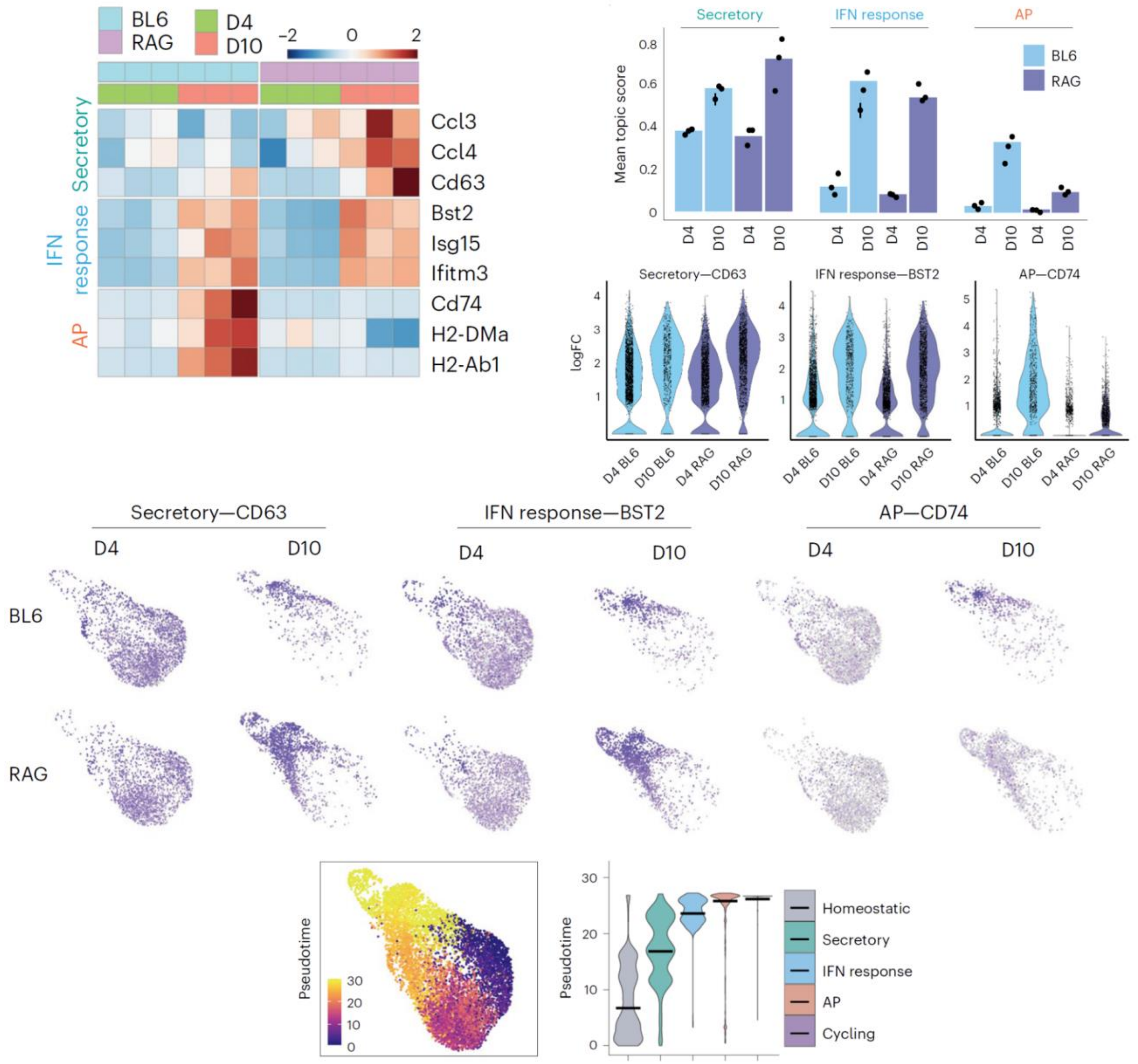

Figure 3.3 Transcriptional analysis of microglia response following T cell infiltration. a, Heat map of log2 fold change (FC) of key markers of the secretory (Secr, top), IFN response (IFNR, middle) and AP (bottom) programmes separated by timepoint and mouse strain. **b**, Bar graph showing the mean topic score for each programme (AP, secretory, and IFN response) in all microglia from each condition. **c**, Violin plots quantifying the expression of key markers of the secretory, IFN response and AP programmes in microglia from each condition. **d**, Feature plots illustrating the distribution of key markers of the secretory, IFN response and AP programmes in microglia. **e**, UMAP plot of pseudotemporal cell ordering results performed using Monocle 3 showing microglia cell state ordering beginning with the homeostatic state (pseudotime 0). Violin plot shows the contribution of each microglia cluster at specific pseudotime values. Microglia cell states are ordered by the median pseudotime value displayed as a black bar.

We performed subset analysis of microglia to determine how their gene expression changes over time in parallel with T cell activation (Fig 3.2b, d). Subclustering of microglia showed similar populations as we previously identified. We scored each microglia in the dataset for its expression of top genes associated with each previously defined topic (Fig 3.2b, d, Table S3), IFN response, secretory, and AP. This showed that all three gene expression programs increase over time from day 4 to 10 in WT animals (Fig 3.3 a, b). At day 4, we observed the highest mean score for the secretory program and lowest for the AP program, suggesting more microglia express the secretory than AP program at the early timepoint. Importantly, we found limited to no expression of the AP program in microglia from RAG1 KO mice that lack T cells (Fig 3.3a-d). In contrast, we found similar expression of the secretory and IFN response programs in RAG1 KO mice, indicating that the AP but not secretory and IFN response programs are dependent on lymphocytes. Top markers of each program showed a similar pattern, where large numbers of microglia express *CD63* (secretory) and *BST2* (IFN response) at day 4 but limited microglia express *CD74* (AP) (Fig 3.3d). We performed pseudotemporal analysis using the Monocle pipeline to further explore the temporal relationship of the microglia programs. This revealed a progression from homeostatic, through the secretory and IFN response, ending in the AP and cycling clusters (Fig 3.3f). These data support a model where microglia initially upregulate the secretory and IFN response programs in response to cancer cell appearance in the brain, followed by upregulation of genes for antigen presentation after lymphocyte infiltration, which may sustain T cell activation locally in the brain and explain why microglia loss results in a diminished T cell response. Of note, we also observe an expansion of immune suppressive cells (Tregs and monocytes) at the later timepoint (day 10)(Fig 3.2c, 3.4c), which may counteract anti-tumor immunity and explain why tumors continue to grow in some animals.

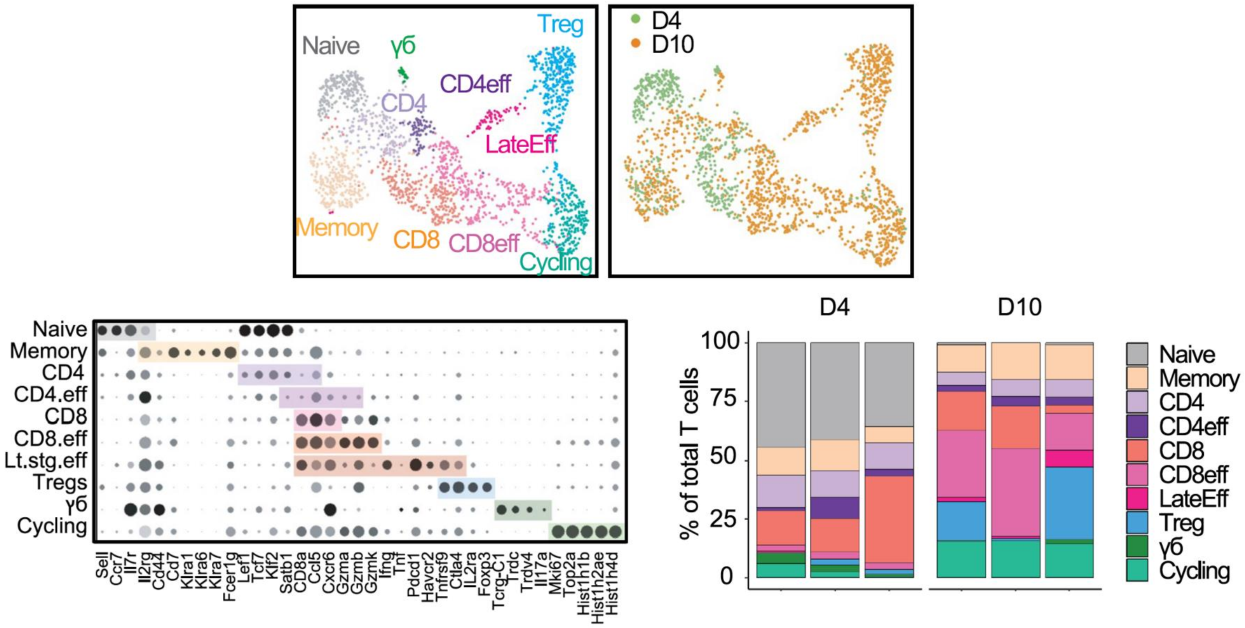

Figure 3.4. Temporal analysis of T cell infiltrates in BCBM. a, UMAPs show T cells (n = 1949 cells) from C57BL/6 mice at day 4 and 10, colored by cluster (left) and timepoint (right). **b**, Dot plot shows expression of top marker genes for each T cell cluster from Fig. 3.4a. CD4.eff = CD4+ effector T cell, CD8.eff = CD8+ effector T cell, Lt.stg.eff = late stage effector T cell, γδ = gamma delta T cell. **c**, Bar graph illustrates the distribution of T cell clusters in each animal (n = 6) separated by timepoint.

The pro-inflammatory response is conserved in human microglia

We investigated the pro-inflammatory response in human microglia and its relevance in BCBM patients. We developed a humanized mouse model of BCBM based on prior work, where MITRG mice (human *CSF1*, *IL3* and *TPO* knock in to *Rag2*$^{-/-}$*Il2rγ*$^{-/-}$ mice) are reconstituted with human microglia and macrophages following transplantation of human induced pluripotency derived hematopoietic progenitor cells (iHPSCs) into the postnatal brain[91–93]. In contrast to patient BCBM samples, we were able to use these animals to investigate the initial response of human microglia to tumor initiation. We injected MITRG mouse pups with GFP-labeled iHPSCs, allowed engraftment for 10 weeks, and injected mCherry-labeled 231BR cells intracardially (Fig 4.1a). Control (n=3) and metastatic (n=3) mice were harvested three weeks later and fluorescence microscopy confirmed the engraftment of GFP$^+$ human

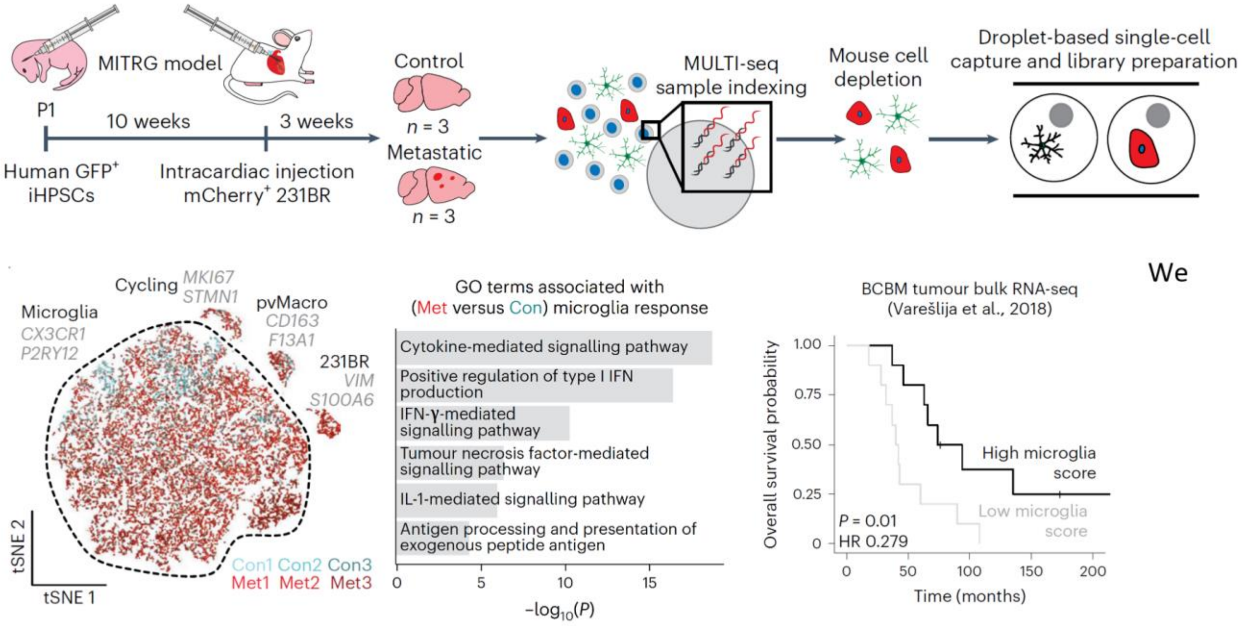

Figure 4.1 The pro-inflammatory response is conserved in human microglia and associated with better prognosis in patients with BCBM. a, Schematic showing experimental design for scRNA-seq of human microglia from humanized MITRG mice transplanted with 231BR cells. MITRG mouse pups were injected with GFP-labelled iHPSCs, aged to 10 weeks and injected intracardiac with mCherry labelled 231BR cells. Brains from control (n = 3) and metastatic (n = 3) mice were digested to single-cell suspensions 3 weeks later. Dissociated cells from each sample were indexed using MULTI-seq. Mouse cells were removed using anti-mouse MHC-I magnetic beads, and recovered cells were pooled into metastatic or control samples for scRNA-seq. **b**, tSNE plot shows human cells (n = 21,353) coloured by mouse and labelled by cell type. Top marker genes (grey) for each cell type were identified using the Wilcoxon rank-sum test. For full marker gene list, see Supplementary Table 6. pvMacro, perivascular macrophages. **c**, Bar plot showing selected top GO terms associated with the human BCBM microglia response signature. Differentially expressed (DE) genes (n = 4,904, adjusted P < 0.05) were determined using the Wilcoxon rank-sum test. GO terms were determined using Enrichr and select upregulated terms with P values <0.05 were retained. For full gene list, see Supplementary Table 6. **d**, Kaplan–Meier plot showing overall survival probability in human patients with BCBM stratified by expression of canonical microglia genes. Bulk RNA-seq data from patient BCBM tumours (n = 20, Varešlija et al.)50 were scored for microglia gene signature and stratified into high and low groups. Scores were determined using the sum of scaled and centered values from log(CPM + 1) transformed data, HR = hazard ratio**.**

microglia and mCherry$^+$ 231BR metastases. Human cells were subsequently isolated and captured for sequencing (Fig 4.1a).

Clustering and marker gene analysis of the 21,353 human cells that passed quality filtering revealed a distinct population of 231BR cells *(VIM)* and several populations of myeloid cells (Fig 4.1b). These included human perivascular macrophages (*CD163*), microglia (*TMEM119, P2RY12)*, and a population of proliferating myeloid cells (*MKI67*). We identified 4,904 genes differentially expressed between microglia from control and metastatic brains (adjusted p<0.05) (Table S6). Gene Ontology (GO) analysis of this BCBM microglia response signature revealed that similar pathways were upregulated in human microglia as observed in mouse, including IFN response, AP, and cytokine signaling pathways (Fig 4.1c). We used gene scoring to further investigate human microglia heterogeneity and expression of the core topics upregulated in mouse BCBM (Fig 4.1d). This showed distinct but overlapping expression of the IFN response, AP, and secretory programs in subsets of human microglia like observed in mouse. Importantly, upregulation of the IFN response and AP topics in this model was not as consistent or robust as observed in mouse microglia. This is consistent with the more severe immune defects in MITRG mice and our findings that T cells are required for complete microglia activation.

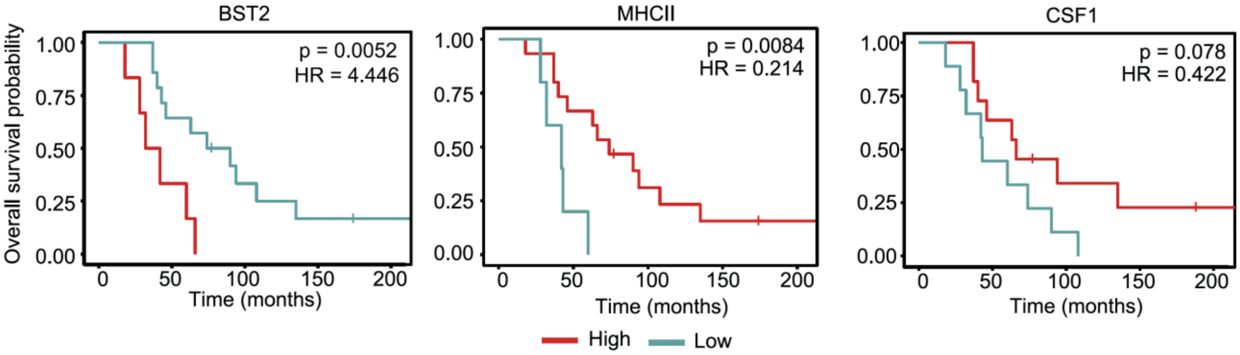

Figure 4.2 Correlation of microglia topics to survival in patient data. Kaplan-Meier plots show overall survival probability stratified by MHC-II, CSF1, and BST2 expression in bulk RNA-seq data from human patient BCBM tumors (Varešlija et al.50).

We subsequently compared the prognostic relevance of microglia signatures in BCBM patients using a bulk RNA sequencing dataset of 20 human BCBM tumors[94]. We found that patients with a high expression of canonical microglia markers had significantly better overall survival (HR=0.279, p=0.01), suggesting increased microglia infiltration is associated with better outcomes (Fig 4.2). We further found that higher expression of key genes characteristic of the AP (MHC-II, p=0.0084) and secretory programs (CSF1, p=0.078) are associated with increased overall survival, while higher expression of the IFN response gene BST2 (p=0.0052) is associated with decreased survival**.** These data suggest that the microglia pro-inflammatory response can be clinically beneficial in patients and support the hypothesis that complete activation of microglia by T cells (i.e., upregulation of the AP program) is a key feature of antitumor microglia, and incomplete activation (i.e., IFN response program only) leads to worse outcomes. In sum, our study supports a model where microglia are critical to support the antitumor immune response in the CNS and suppress BCBM (Fig 4.3).

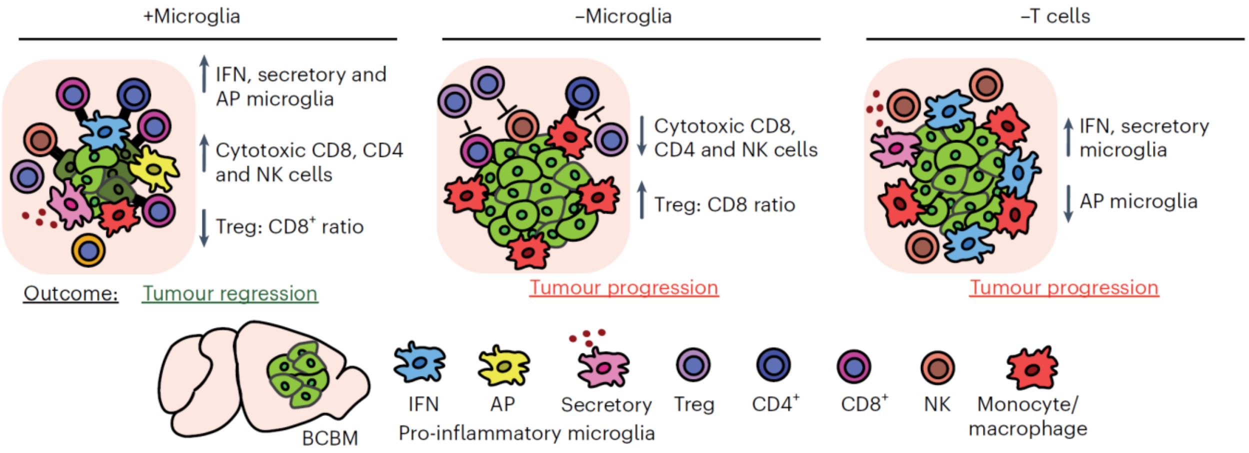

Figure 4.3 Model for role of microglia in promoting anti-tumour immunity. In microglia-replete conditions (+Microglia), microglia respond to BCBM by upregulating pro-inflammatory programmes (IFN response, AP and secretory) that promote anti-tumour CD4, CD8 and NK cell responses and tumour regression in the CNS. In microglia-depleted conditions (−Microglia), NK and T cell responses are deficient and the proportion of Tregs is increased, resulting in tumour progression. In animals lacking T cells (−T cells), microglia fail to upregulate AP genes and tumour regression is not observed, suggesting that T cells are required for complete microglia activation and that reciprocal microglia–T cell activation is critical for tumour suppression.

Enhancement of parenchymal AP activity promotes tumor rejection.

To determine if the AP activity of microglia may be leveraged for a more robust rejection of BCBM, we utilized an agonistic anti-CD40 antibody (aCD40) to drive a more robust AP phenotype in microglia and alternate CNS APCs. Following intracardiac injection of tumors, aCD40 or IgG isotype control antibody was administered, intracranially, and tumor growth was monitored by IVIS (Fig 5.1a). Upon reaching humane endpoint, the immune repertoires were evaluated by flow cytometry for subtype phenotyping and markers of activation. We observed greater survivability of the aCD40-treated group relative to control, paired with lower tumor-derived radiance detected *in vivo* (Fig5.1b, c, p=0.0075). *Ex vivo* radiance confirmed this effect, indicating that the aCD40 treatment had a marked effect on brain parenchymal tumor growth (Fig 5.1d).

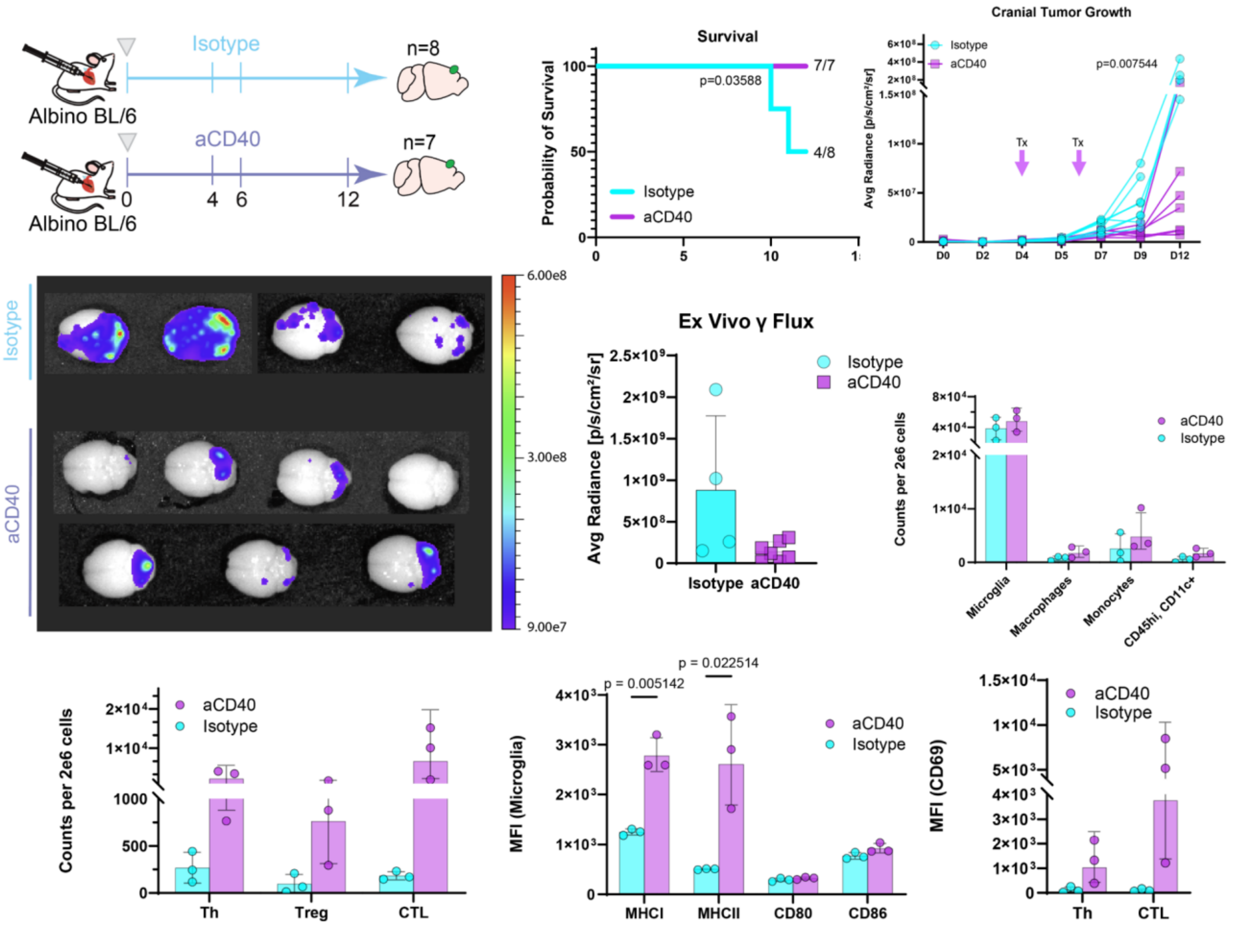

Figure 5.1 APC enhancement improves survival and drives tumor rejection in BCBM. a, Schematic of experimental design comparing tumor growth and leukocyte activation in Albino BL/6 mice following treatment with Isotype control (*n*=8) or agonistic αCD40 (*n*=7) at 4- and 6-days post tumour implantation. Mice were injected intracardially with 500,000 EO771 GFP-Luc cells and imaged for luminescence on days 0, 2, 4, 5, 7, 9, and 12. **b**, Kaplan–Meier plot shows survival in isotype (4/8, 50%) and αCD40 (7/7, 100%) treated mice. P value determined by log-rank (Mantel–Cox) test. **c**, *In vivo* tumour growth as measured by IVIS in average radiance (p/s/cm^2/sr). Arrows indicate timing of isotype or αCD40 treatment. P value determined by Mixed-effects model with the Geisser-Greenhouse correction. **d**, IVIS imaging of *ex vivo* EO771 luciferase luminescence signal between isotype and αCD40 treated mice. (Left) Ex vivo whole brain luminescence images show signal from tumor cells in each tissue at day 12. (Right) Bar graph shows quantification of luminescence in average radiance (p/s/cm^2/sr). **e**, Quantification of myeloid populations between isotype and αCD40 treated mice by flow cytometry. CD45$^{hi\text{-}int}$ CD11b+ myeloid cells were identified following gating for live (Sytox negative) singlets. Error bars represent mean +/− standard deviation. Pairwise comparisons of counts between groups were not significant. **f**, Quantification of lymphoid populations between isotype and αCD40 treated mice by flow cytometry. CD3$^+$CD11b$^-$ MHCII$^-$ CD19$^-$ T cells were identified following gating for live (AmCyan negative) singlets. Error bars represent mean +/− standard deviation. **g**, Expression of AP and costimulatory machinery by microglia from Fig 5.1a. Error bars represent mean +/− standard deviation. P values shown are the result of an unpaired two-sided Student's t-test. **h**, Expression of activation markers by T cell subsets from Fig 5.1a. Error bars represent mean +/− standard deviation. Pairwise comparisons of counts between groups were not significant.

Analysis of the immune repertoire showed that aCD40 impact had minimal impact on the composition of the myeloid compartment, demonstrating a small but nonsignificant increase in microglia (CD45lo, CD11b+), macrophages (CD45+, CD11b+, F4/80+, Ly6c-) monocytes (CD45+, CD11b+, F4/80lo, Ly6c+), and a CD45+, CD11b+, CD11c+ population that could be classified as either dendritic cells or damage-associated microglia (DAMs)(Fig 5.1e). This activity implies that the reduction in tumor growth we observed was likely not attributed to a change in myeloid cell infiltration or activation, but more directly to the aCD40 effect on cell activity. Changes in the lymphoid repertoire were more pronounced, with a robust expansion of helper (Th, CD3+, CD4+, FoxP3-) and regulatory (Treg, CD3+ CD4+, FoxP3+) T cells as well as a 20-fold expansion of CD3+, CD8+ cytotoxic lymphocytes (CTL) (Fig 5.1f). Interrogation of AP (MHC I, MHC II) and T cell costimulatory molecules (CD80, CD86) on the microglia population show an upregulation of both class I (p=0.0051) and class II (p=0,.0225) antigen presentation that persists for 6 days following aCD40 treatment (Fig 5.1g), however this activity is uncoupled from the expected enhancement of CD80/86 costimulation. Activation of effector T cell populations, as measured by CD69 expression, was also robustly upregulated in all aCD40 treated animals (Fig 5.1h). Furthermore, the apparent exclusion of tumor signal at the site of treatment injections in the forebrain suggests a local effect of parenchymal APCs, the most abundant of whom are microglia.

Summary and Conclusions

We utilized scRNA-seq, genetic and humanized mouse models to investigate the role of microglia in mouse and human BCBM. Our scRNA-seq analyses revealed that mouse microglia upregulate three core pro-inflammatory programs in response to BCBM, designated as IFN response, AP, and secretory. We validated key pro-inflammatory markers at the protein level in three different models of BCBM, using flow cytometry, multiplex IF, and cytokine array. Using the FIRE-KO model, we found that animals lacking microglia demonstrate less capacity for tumor regression due reduced anti-tumor T and NK cell responses. T cell depletion experiments revealed that complete microglia activation and tumor regression are not observed in the absence of T cells, suggesting that reciprocal microglia-T cell activation is critical for tumor suppression. Finally, we used a humanized mouse model to show that human microglia upregulate similar pro-inflammatory response programs in response to BCBM and found that markers of complete microglia activation are associated with better prognosis in BCBM patients. This pro-inflammatory, tumor suppressive role of microglia contrasts with the anti-inflammatory, pro-tumorigenic role previously ascribed to microglia and other TAMs and raises the prospect of targeting microglia to treat BCBM.

An interesting phenomenon revealed by our study is the opposing effects on metastatic progression observed using TAM depletion strategies versus germline genetic ablation of microglia using the FIRE-KO mice. While we found that mice lacking microglia develop increased disease burden, previous work clearly showed decreased tumor progression following TAM depletion with CSF1R inhibitors or genetic ablation using CX3CR1-targeted mouse models[20,22,95]. There are several possible explanations for these different outcomes. It is clear that microglia depletion in the FIRE-KO model is more complete and more restricted to microglia than other approaches[24]. Furthermore, microglia cannot rebound and repopulate the brain or become reprogrammed as has been observed in other depletion models[96,97]. The massive cell death produced in the Cx3cr1$^{CreERT/+}$:ROSA26i$^{DTR/+}$ depletion model has also been shown to induce cytokine storm and astrogliosis, which may have confounding effects on tumor growth and the immune response[98,99]. Another important distinction in our study is that the FIRE-KO mice lack microglia from birth, while most prior studies targeted TAMs postnatally and after tumor initiation. It is therefore plausible that the timing of depletion impacts the outcome, as microglia and TAMs may become tumor-promoting as disease progresses.

It will be important in future work to investigate the mechanism by which microglia support anti-tumor T cell responses in the CNS. We found that pro-inflammatory microglia secrete several chemokines that could promote T cell trafficking to the CNS, such as CCL5, CXCL9 and CXCL10 (Fig 1.8). Pro-inflammatory microglia also upregulate AP machinery (Fig 1.4), which could enable them to present tumor neoantigens to CD4 or CD8 T cells to sustain T cell activation locally in the brain. Leveraging this activity though CD40 agonism enhancing local antigen presentation demonstrated therapeutic benefit in BCBM bearing mice that may be plausible for patients (Fig 5.1). Localization of tumor clearance in the forebrain using our mouse model indicates that diffusion is likely a factor in efficacy of such treatment. While intrathecal or peripheral administration of aCD40 may be less invasive, higher dosing may be necessitated and as such, single agent therapy may not be realistic. Precedent exists for transmeningeal administration of treatment in clinical cases of epilepsy which may offer alternatives to high systemic dosing necessary for intracranial efficacy[27, 28]. Nonetheless, further work to understand how microglia drive anti-tumor immunity and why they ultimately fail to control disease progression is imperative to inform new treatment and improve prognoses of patients worldwide.

Methods

Research within this publication complies with relevant ethical regulations. Animal studies were performed in accordance with an Institutional Animal Care and Use Committee (IACUC)-approved protocol #AUP-19-051 at the University of California Irvine. Human formalin-fixed paraffin-embedded samples were exempted by institutional review board as human subjects research due to patient de-identification.

Normal human brain and human BCBM samples

FFPE sections of deidentified normal human brain and resected breast cancer brain metastasis were acquired from University of California Irvine department of Pathology and Laboratory Medicine, experimental tissue shared resource facility and the University of California Davis Pathology Biorepository.

Cell lines

MDA-MB-231-Br2[65] cells stably transduced with membrane targeted AcGFP (rLV.EF1.AcGFP1-Mem-9, ClonTech/Takara Bio, USA, Cat#0019VCT), mCherry (rLV.EF1.mCherry-9, ClonTech/Takara, Cat#0037VCT), and luciferase lentivirus were a generous gift from Ian Smith (Parker, 2017, Bos, 2009). 4T1 cells were purchased from ATCC (ATCC Cat# CRL-2539, RRID:CVCL_0125), stably infected with GFP lentivirus (Santa Cruz Biotechnology, copGFP Control Lentiviral Particles, Cat#sc-108084) at a MOI or 10, and sorted for GFP expression after two weeks growth in culture. EO771 cells were purchased from CH3 Biosystems (Cat. No. 94A001, RRID:CVCL_GR23) and stably infected with pCDH-EF1a-eFFly-eGFP) lentivirus particles. pCDH-EF1a-eFFly-eGFP was a gift from Irmela Jeremias (Addgene plasmid #104834; http://n2t.net/addgene:104834; RRID:Addgene_104834). To produce lentiviral particles, HEK293T cells were transfected with pCDH-EF1a-eFFly-eGFP together with pMD2G and psPAX2 packaging plasmids using Lipofectamine 2000 (Invitrogen, Cat# 11668027). Supernatants containing lentiviral particles were used to infect EO771 cells overnight in the presence of 8 µg/ml polybrene (Sigma-Aldrich, Cat# TR-1003-

G). Transduced EO771 cells were sorted on the basis of GFP expression on a BD FACSAria Fusion cell sorter. MDA213-BRm and 4T1 cell lines were cultured in DMEM, 5% FBS, 10U/ml penicillin, 0.1mg/mL streptomycin (GE Healthcare Cat#SV30010), at 37 °C, 5% CO$_2$, 95% relative humidity. EO771 cells were cultured in RPMI 1640, 5% FBS, 10U/ml penicillin, 0.1mg/mL streptomycin, 10mmol/L HEPES at 37 °C, 5% CO$_2$, 95% relative humidity. Cells were passaged for one-two weeks prior to intracardiac or intracranial injections. All cell lines were authenticated by short tandem repeat analysis by ATCC prior to injection.

Mouse strains

Female Foxn1$^{nu/nu}$ mice (IMSR Cat# JAX:007850, RRID: IMSR_JAX:007850), FVB (IMSR Cat# JAX:001800, RRID:IMSR JAX:001800), C57BL/6J (IMSR Cat# JAX:000664, RRID: IMSR_JAX:000664), B6(cg)-Tyrc-2J/J (IMSR Cat# JAX:000058, RRID:IMSR JAX: 000058, albino B6), BALB/cJ (IMSR Cat# JAX:000651, RRID:IMSR_JAX:000651) and B6.129S7-Rag1$^{tm1Mom/J}$ (RAG1-KO) were purchased from The Jackson Laboratories. Female MITRG mice (IMSR Cat# JAX:017711, RRID: CVCL_JM19) which are C:129S2-Rag2$^{tm1.1Flv}$ Csf1$^{tm1(CSF1)Flv}$ CSF2/IL3$^{tm1.1(CSF2,IL3)Flv}$ Thpo$^{tm1.1(TPO)Flv}$ Il2rg$^{tm1.1Flv}$/J were bred, housed and maintained by the laboratory of Mathew Blurton-Jones (IACUC protocol #AUP-17-162). *Csf1r*$^{\Delta FIRE/\Delta FIRE}$ (FIRE-KO) and *Csf1r*$^{FIRE/FIRE}$ (FIRE-WT) mice were a gift from Claire Pridans and Mathew Blurton-Jones laboratories and were housed and maintained by the Lawson laboratory. All animals were aged between 5-15 weeks old. When possible, animals were randomized between cages and ages prior to injection of cells or PBS. Only female animals were included in these studies because breast cancer predominantly afflicts women. All animal studies were performed in accordance with an IACUC approved protocol #AUP-19-051 at the University of California Irvine.

Immunofluorescence analysis of human BCBM samples

4-µm sections were heated at 65 °C for 30 min, then deparaffinized by two sequential five-min incubations in Histo-Clear (National Diagnostics, #HS-200, Atlanta, Georgia, USA). Tissues were rehydrated with graded solutions of ethanol (100%-50%) and washed in double-distilled H_2O and 1XPBS. Antigen retrieval was performed using a microwave pressure cooker with 10 mM citric acid buffer (0.05% Tween-20, ThermoFisher Scientific Cat#BP337500, pH 6.0). Tissues were blocked in blocking solution (0.1% Tween-20 and 10% Goat Serum in PBS) for 30 min at room temperature, incubated with primary antibodies diluted in blocking solution at 4 °C overnight, washed in PBS, incubated with secondary antibodies diluted in blocking solution for one hour at room temperature, and washed in PBS. Slides were mounted with VECTASHIELD Antifade Mounting Medium with DAPI (Vector Laboratories, #H-1200, Burlingame, California, USA) and micrographs were taken with the BZ-X700 Keyence fluorescence microscope.

Generation of BCBM in mice

For intracardiac injection to establish brain metastasis, as previously described by Campbell et al, 2012[102], cells were injected into the left cardiac ventricle of anesthetized mice (300mg/kg Avertin). For 231BR brain metastasis 500,000 cells in 100µL of DPBS were injected into nine week old Foxn1$^{nu/nu}$ or 10 week old MITRG mice. For 4T1 brain metastasis, 100,000 cells were injected into nine week old BALB/cJ mice in 100µL of DPBS. For the intracranial injection of FVB, C57BL/6, FIRE-WT, FIRE-KO, RAG1-KO or albino B6, 100,000 VO-PyMT, EO771, or Py8119 cells were injected in 10 µL PBS to a depth of 3mm into the right coronal suture of five-week-old mice[18,20]. Control mice were injected with 10 µL PBS. Injections were replicated in 2-3 cohorts of 4-6 mice and in different mouse strains to ensure reproducibility of results.

Dissection and visualization of mouse BCBM by whole mount fluorescence microscopy

At endpoint, mice were euthanized and perfused with 50mL of sterile ice cold 1X PBS, 1mg/mL EDTA. The brain was dissected from the cranium and meninges, and then washed in ice cold sterile 1X PBS. To visualize metastasis prior to RNAseq, flow cytometry analysis, or fixation, the whole brain was placed on the dissection microscope (Leica Biosystems, DMC 2900) and imaged for GFP fluorescence and brightfield.

Mouse brain fixation and sectioning

Dissected brains were drop fixed into 4% PFA, 1X PBS, pH 7.4 overnight at 4°C. Fixed brains were transferred into 30% Sucrose 1X PBS for 24 hours prior to cryosectioning on sliding microtome (Leica Biosystems, SM2010R). Brains were frozen onto the stage for sagittal or coronal sectioning at 40µm thickness using dry ice powder. Serial slices were collected into 1X PBS, 0.05% sodium azide and stored at 4°C for floating section immunostaining.

Immunofluorescence staining of floating sections

Brain slices were transferred into a well of a 24 well plate containing 300µL of blocking solution (1X PBS, 5% serum, 0.3% tritonX-100) and placed on an orbital shaker for one hour. Blocking solution was removed and replaced with 500µL of primary antibody diluted in blocking solution and incubated overnight on an orbital shaker at 4°C. The next day, primary antibody was removed, and brain slices were washed with three sequential 500µL washes of blocking solution and incubated with secondary antibody for one hour at room temperature. Brain slices were transferred to a glass slide and mounted with VECTASHIELD Antifade Mounting Medium with DAPI (Vector Laboratories, # H-1200, Burlingame, California, USA). Micrographs were taken with the BZ-X700 Keyence fluorescence microscope and acquisition software. Primary antibodies: Rabbit polyclonal anti-IBA1 diluted 1:500 (RRID: AB_A39504

Wako Cat#019-19741); Secondary antibodies diluted 1:400: Goat anti-rabbit IgG conjugated with Alexa Fluor 568 and 488 (ThermoFisher Scientific, RRID: AB_2535730 Cat#A21069 and RRID: AB_2576217 Cat#A11034); Goat anti-rat IgG conjugated with Alexa Fluor 568 and 647 (RRID: AB_2534074 Cat#A11006and RRID: AB_141778 Cat#A21247); Goat anti- hamster conjugated with Alexa Flour 647 (RRID: AB_2535868 Cat#A21451) (Thermo Fisher Scientific Inc., Carlsbad, California, USA).

Quantification of IBA1 immunofluorescence in Foxn1$^{nu/nu}$ brains

Four brain tissue sections from control (n=4) and 28-day metastatic (n=4) Foxn1$^{nu/nu}$ mouse brains were stained for IBA1. Micrographs were acquired on the BZ-X700 Keyence fluorescence microscope. Baseline exposure level for IBA1 was established using control brain tissues under 20X magnification. For controls, 8 x 16 µM Z-stack fields of brain parenchyma per mouse were taken. For 231-BR metastatic brains, AcGFP^{+} lesions were located at low magnification (2X), then images at 20X using the same exposure setting as control. Z-stack micrographs were compressed into maximum intensity projection and opened in FIJI (Fiji, RRID:SCR_002285). Images were quantified for the number of IBA1+ cells in 8-17 fields from 4 control and 4 metastatic mouse brains using the threshold, convert to binary, watershed, and analyze particles functions. Data was tabulated and analyzed in GraphPad Prism 8 (https://www.graphpad.com/scientific-software/prism/, GraphPad Prism, RRID:SCR_002798).

CODEX Imaging of Mouse BCBM

C57BL/6 control or EO771-GFP tumor bearing mouse brain tissue was fixed in 4% PFA overnight, cryoprotected in 30% sucrose 1X PBS until tissue equilibrated, then embedded in OCT and frozen for sectioning to 10 micron thickness and mounted on Poly-L lysine coated glass coverslips and stored at -

80°C prior to staining with CODEX oligo barcoded antibodies. Reporter plate containing complementary fluorescent oligo barcodes was prepared according to the CODEX manual Rev. C. Tissues were stained with all antibodies (see below) simultaneously following CODEX manual rev. C, and imaged using 20X PlanApo 0.75 NA lens using the CODEX automated imaging system with the Keyence 700 microscope and BZX software. A 7X7 tile scan with 6x Z planes 1.5u steps was taken, and processed using the CODEX processor 1.8 to perform deconvolution, background subtraction, stitching, and compression. The output qptiff images were segmented in QuPath using StarDist (https://github.com/stardist/stardist). Segmented cells were phenotyped by a user trained machine learning classifier in QuPath based on the marker expression for TMEM119, IBA1, MHC-II, CD74, ISG15. Two tumor distal and two tumor proximal regions from four mice were imaged, segmented and phenotyped and showed consistent frequencies of cell types. The following antibodies, barcode/ reporter and fluorescence combinations were used: TMEM119 (195H4, Synaptic Systems) BX/RX035-ATTO550, MHC-II (M5/114.15.2, Akoya) BX/RX001-ATTO550, ISG15 (1H9L21, Thermofisher) BX/RX045-CY5, CD74 (ln1/CD74, Biolegend) BX/RX036-CY5, IBA1 (019-19741, Wako) BX/RX042- CY5. Custom conjugations of TMEM119, ISG15, CD74 and IBA1 were performed using the Akoya custom conjugation kit and barcodes, following the CODEX manual, and validated by SDS-PAGE and visual assessment of staining compared to standard immunofluorescence with unconjugated antibody and fluorescent secondary antibody on FF mouse spleen or tumor sections.

Isolation of cells for scRNA-seq

Single cell suspensions from mouse brains were prepared using the Adult Brain Dissociation Kit, Mouse and Rat (Miltenyi Biotec) with some modifications. Whole dissected brains were chopped into 8 pieces of equal size and placed into C tube (Miltenyi Biotec, Cat#130-093-237) containing enzyme P and A (Foxn1$^{nu/nu}$ mice) or 1mg/mL Collagenase D (Millipore Sigma Cat#11213857001, C57BL/6 and RAG1-KO mice. Brain tissue was digested using gentleMACS Octo Dissociator with heaters operating the 37°C adult brain dissociation protocol for 30 minutes. After digestion, the cell suspension was strained over a sterile 70µm strainer (Fisher Scientific, Cat#22363548) and washed with 5mL FACS buffer containing ice cold DMEM/F12, 50mM HEPES, and 2% BSA. After removal of myelin by density centrifugation, the cell pellet was washed and remaining red blood cells were lysed with red blood cell lysis buffer. Cells were then re-suspended in FACS buffer and blocked with anti-CD16/32 for 15 minutes on ice. Next, cells were stained with fluorescent antibodies on ice for 15 minutes shielded from light. C57BL/6 and RAG1-KO cells from individual mice were labeled using a CellPlex multiplexed oligo labeling kit in accordance with the manufacturer's protocol (10x Genomics Cat# 1000261). The labeled cells were washed with 500µL of FACS buffer and resuspended in 500µL of FACS buffer, strained through 40µm strainer prior to sorting on BD FACSAria Fusion sorter. For sorting of microglia, astrocytes, cancer cells, and total leukocytes, cells were gated for size based on forward and side scatter, single cells, and Sytox Blue viability (Thermofisher, Cat#S34857. All myeloid cells ($CD45^+$ $CD11b^+$) and astrocytes ($CD45^-$, $ACSA2^+$) were sorted from control and metastatic mouse brains into 500µL of chilled FACS buffer. GFP^+ 231BR cells were sorted from metastatic brains into 500µL of FACS buffer. Total leukocytes ($CD45^+$) were sorted from tumor-bearing control and RAG1-KO mouse brains into 500µL of FACS buffer.

scRNA-seq of murine brain leukocytes

FACS isolated mouse immune cells were centrifuged for 10 minutes at 300g and washed with 0.04% BSA in PBS. A power analysis was performed to estimate the number of cells needed for capture for barcoding for scRNA-seq and identified 5,000- 10,000 cells per mouse. Cells were resuspended to achieve approximately 1,000 cells/µL. Final cell suspensions were counted on the Countess II automated cell counter to determine actual concentration for droplet generation. Cells were loaded onto the 10x Genomics Chromium Single Cell Gene Expression 3’ v2 Chemistry kits for GEMs generation. Following the Chromium Single Cell 3’ Reagents Kits version 2 user guide (CG00052 Rev B), cells were loaded to achieve approximately 10,000 cells for capture. Libraries were sequenced on the Illumina HiSeq 4000 (Foxn1$^{nu/nu}$) or NovaSeq 6000 (C57BL/6, RAG1-KO) platform to achieve an average of read depth of 50,000 mean reads per cell. Sequencing reads were aligned utilizing 10x Genomics Cell Ranger Count 3.0.2 to a dual indexed GRCh38 and mm10 reference genome.

Flow cytometry analysis of immune cells from control and BCBM mouse brain tissue

For flow cytometry analysis of metastatic mouse brains, tissue was prepared as for FACS sorting, with the exception that 1mg/mL Collagenase D (Milipore Sigma Cat#11213857001) was used for digestion instead of enzyme P provided in the Adult Brain Dissociation kit. After a single cell suspension was obtained, cells were stained with ZombieNIR viability dye (1:500, BioLegend Cat. No. 423106) in 50µL of ice-cold PBS for 15 minutes. Cells were washed with FACS buffer and blocked with anti-CD16/32 antibody diluted in FACS buffer for 15 minutes on ice. Next, cells were stained with fluorescent antibodies for extracellular markers for 15 minutes on ice, protected from light. Cells were washed with 500µL FACS buffer and resuspended in 400µL FACS buffer, strained through a 40µm cell strainer and analyzed using BD Fortessa X20. For intracellular staining of Foxp3 and CD3e, cells were fixed with the eBioscience Foxp3 /Transcription Factor Staining Buffer set according to the manufacturer's instructions (Thermofisher Cat #00-5523-00) and stored at covered in the dark at 4°C for <2 days before analysis on the BD Fortessa X20. The following antibodies were used for flow cytometry analysis: CD45-BV510 (Biolegend, 30-F11, 1:100), CD45-FITC (Biolegend, 30-F11, 1:100), CD11b-BV605 (Biolegend, M1/70, 1:200), CD11b-PE (Biolegend, M1/70, 1:200), CD11b-BV650 (Biolegend, M1/70, 1:200), ACSA-2-APC (Miltenyi, REA969, 1:80), Ly6C-BV785

(Biolegend, HK1.41:200, 1:200), Ia/Ie (MHC-II)-PacificBlue (Biolegend, M5/114.15.2, 1:500), CD74-AF647 (Biolegend, In1/CD74, 1:100), CD317-PE (Biolegend, 129C1, 1:100), CD3-PerCPCy5.5 (Biolegend, 17A2, 1:100), TCRb-PECy5 (Biolegend, H57-597, 1:100), NK1.1-PEDazzle594 (Biolegend, PK136, 1:100), CD4-BV605 (Biolegend, RM4-5, 1:500), CD8a-PacificBlue (Biolegend, 53-6.7, 1:500), Foxp3-PE (eBioscience, FJK-16s, 1:100), CD152 (CTLA-4)-APC (BD, UC10-4F10-11, 1:100), CD44-PECy7 (Biolegend, IM7, 1:100), CD62L-BV785 (Biolegend, MEL-14, 1:100), CD107a-FITC (Biolegend, 1D4B, 1:100).

In vitro **differentiation and early postnatal transplantation of iHPCs**

Differentiation of Hematopoietic Progenitor Cells from iPSCs (iHPCs) performed according to McQuade et al. (2018)[91]. Briefly, iPSCs were first passaged in mTeSR-E8 and on day 0, cells were transferred to Medium A from the STEMdiff Hematopoietic Kit (Stem Cell Technologies, Cat#05310). On day three, flattened endothelial cell colonies were transferred to Medium B for seven additional days while iHPCs began to lift off the colonies. On day 10, non-adherent CD43$^+$ iHPCs were collected by removing medium and cells and at this point, d10-d11 iHPCs can be frozen in Bambanker (Fisher Scientific, Cat#NC9582225) for later transplantation. Cells used for early-postnatal iHPC transplantation were thawed in iPS-Microglia medium (DMEM/F12, 2X insulin-transferrin-selenite, 2X B27, 0.5X N2, 1X glutamax, 1X non-essential amino acids, 400 mM monothioglycerol, and 5 mg/mL human insulin freshly supplemented with 100ng/mL IL-34, 50ng/mL TGFb1, and 25 ng/mL M-CSF (Peprotech, Cat#100-21) according to McQuade et al, 2018[52] and allowed to recover for 24 h. Early Postnatal Intracerebroventricular Transplantation of iHPCs was performed as described in Hasselmann et al, 2019[92]. Briefly P1 to P2 MITRG mice placed on ice for two-three min to induce hypothermic anesthesia. Free-hand transplantation was performed using a 30-gauge needle affixed to a 10µL Hamilton syringe, mice received 1µL of iHPCs suspended in sterile 1X DPBS at 31.25-62.5K cells/µL at each injection site (8 sites) totaling 250-500K cells/pup. Bilateral injections were performed at 2/5th of the distance from the lambda suture to each eye, injecting into the lateral ventricles at 3mm and into the overlying anterior cortex at 1mm, and into the posterior cortex in line with the forebrain injection sites, and perpendicular to lambda at a 45° angle. Transplanted pups were then returned to their home cages and weaned at P21.

Isolation of human xenotransplanted microglia

At 10 weeks old, MITRG mice were injected intracardially with 500,000 mCherry labeled 231BR cells as previously described. 25 days after intracardiac injection and following perfusion with ice cold PBS containing 5µg/ml actinomycin D (act D, Cat#A1410), whole metastatic brains were briefly imaged on a dissection microscope (Leica Biosystems, DMC 2900) for mCherry and GFP intensity. Half brains were then dissected, fixing the left hemisphere in 4% PFA for histology and the right hemisphere was prepped for dissociation as described in Hasselmann et al, 2019[92] with modifications. The cerebellum was removed and the whole right hemisphere was stored briefly in RPMI 1640 containing 5µg/mL act D, 10µM triptolide (Sigma-Aldrich, Cat#T3652), and 27.1ug/mL anisomycin (Sigma-Aldrich, Cat#A9789). Tissue dissociation was then performed using the Tumor Dissociation kit, human (Miltenyi Biotec) and the gentleMACS OctoDissociator with heaters (Miltenyi Biotec) according to manufacturer guidelines with modifications. Briefly, tissue was cut into ~1mm pieces and placed into the C-tubes with the kit's enzymes, 5µg/mL act D, 10µM triptolide, and 27.1ug/mL anisomycin and samples were dissociated using the preprogrammed soft tumor protocol. Following enzymatic digestion, samples were strained through a 70µm filter and pelleted by centrifugation. Myelin and debris were removed by resuspending the pellet in 8mL 23% Percoll (GE Healthcare, Cat#45-001-748), overlaid with 2mL of 1X DPBS, spinning at 400xg for 25 minutes at 4°C, with acceleration and brake set to 0, and discarding the myelin band and supernatant.

MULTI-seq labeling and scRNA-seq of human microglia

For barcoding of cells from each individual mouse the MULTI-seq lipid- tagged indices for sample multiplexing for scRNAseq protocol was followed[101]. Lipid anchor and co-anchor reagents were a generous gift from Zev Gartner, and barcode index oligos were purchased from Integrated DNA Technologies, Inc. Cells were resuspended and washed with 15 mL cold DPBS and pelleted by centrifugation (10 minutes, 400xg). The supernatant was discarded, and cells were resuspended in 180µL of DPBS. 20µL of 20µM Anchor:Barcode solution was added to a final concentration of 2µM, and incubated on ice for five minutes. Next 20µL of 20µM Co-Anchor solution was added, gently mixed and incubated for five minutes. After incubation 1mL 1% BSA in DPBS was added and cells were pelleted by centrifugation (five minutes, 400xg). Finally, the supernatant was removed and washed a second time with 1mL 1% BSA in PBS and pelleted by centrifugation (5 minutes, 400xg). Next, mouse cell removal was performed by resuspending cell pellets in 160µL FACS buffer (0.5% BSA in 1X DPBS) + 40µL Mouse cell removal beads (Miltenyi Biotec) and incubated at 4°C for 15 minutes. Mouse and human cells were then separated using LS columns and the MidiMACs separator (Miltenyi Biotec) and the human cells were collected in the flow through. Human cells were pelleted via centrifugation (10 minutes, 400xg) and control samples and metastatic samples were then pooled separately. Cells were resuspended to ~1,000 cells per microliter in FACS buffer, according to counts performed on a hemocytometer.

ScRNA-seq of MITRG human microglia

Final cell suspensions were counted on the Countess II automated cell counter to determine actual concentration for droplet generation. Cells were loaded onto the 10x Genomics Chromium Single Cell Gene Expression 3' v3 Chemistry kits for GEMs generation. Following the Chromium Single Cell 3' Reagents Kits version 3 user guide (CG000183 Rev C), cells were loaded to achieve approximately 10,000 cells for capture. MULTI-seq barcode libraries were prepared according to the MULTI-seq protocol[103]. Libraries were sequenced on the Illumina NovaSeq 6000 platform to achieve an average read depth of 50,000 mean reads per cell for 3' gene expression libraries. MULTI-seq barcode libraries were sequenced to achieve at least 5,000 reads per cell. Sequencing reads were aligned utilizing 10x Genomics Cell Ranger Count 3.1.0 to a dual indexed GRCh38 and mm10 reference genome. All libraries were aggregated using 10x Genomics Cell Ranger Aggr 3.1.0, to normalize the number of mean reads per cells. MULTI-seq reads were processed according to the MULTI-seq protocol (https://github.com/chris-mcginnis-ucsf/MULTI-seq).

Analysis of BCBM in FIRE mice

Four to six-week-old *Csf1r*$^{\Delta FIRE/\Delta FIRE}$ (FIRE-KO) and *Csf1r*$^{FIRE/FIRE}$ (FIRE-WT) mice were injected intracranially in the right coronal suture with 100,000 enhanced GFP and luciferase labeled EO771 cells as previously described. To monitor brain tumor growth *in vivo*, mice were imaged for luciferase luminescence one day after injection, and every three days thereafter until endpoint. Imaged mice were anesthetized via isoflurane inhalant and administered 300µg D-Luciferin (Goldbio), intraperitoneally, in sterile DPBS. Following a 10-minute incubation, mice were imaged for bioluminescence for six minutes utilizing an IVIS Lumina III In Vivo Imaging System (Xenogen). Regions of interest were selected around each brain and average photon flux (total photons/s-cm^2) was recorded using Living Image analysis software (**RRID:SCR_014247,** http://www.perkinelmer.com/catalog/category/id/living%20image%20software) and average background flux subtracted. At endpoint mice were weighed, euthanized and dissected and the whole brains were removed and placed in a 24 well tissue culture plate submerged in ice cold PBS with D-Luciferin (1.5 mg/mL, Goldbio, Cat# LUCK-1G). After 10 minutes incubation, whole brains were removed from the solution and placed on a black plastic card and imaged for luminescence for 1 second.

A region of interest was drawn around each brain and the total flux (ptotal photons/s-cm^2) was recorded for analysis.

Fingolimod (FTY720) HCL dosing

200 mg of FTY720 was purchased from Selleckchem (Cat. no. S5002) and dissolved in 1mL of DMSO to prepare a 200X stock. To prepare working aliquots, 25uL of stock was dissolved in 5mL of normal saline for a final concentration of 1mg/mL FTY720 (0.001% DMSO). Vehicle was prepared by adding 25uL of DMSO to 5mL normal saline for a final concentration of 0.001% DMSO. Mice were weighed and injected intraperitoneally with 50-100uL of vehicle or 5mg/kg FTY720 immediately before intracranial injection with 70,000 EO771 eGFP eFFly cells, and daily for the duration of the experiment. The experimental groups were blinded when performing intracranial injections of EO771 cells.

Cytokine screen of Microglia

Control and 14-day EO771 eGFP eFfly tumor bearing brains were digested into single cell suspension as previously described for flow cytometry analysis of microglia. Cells were stained for flow cytometry analysis using the markers BV510-CD45 (Biolegend clone 30-F11, 1:100), BV605-CD11b (Biolegend clone M1/70, 1:200), BV785-Ly6C (Biolegned clone HK1.4, 1:200), and PE/Dazzle594-NK1.1 (Biolegend clone PK136, 1:100). 50,000 microglia per sample were FACS sorted based on CD45lo, CD11b+ Ly6C- NK1.1- expression into FACS buffer. After FACS, cells were resuspended in 100uL of 150mM sodium chloride, 1%NP-40 50mM Tris pH 8.0 cell lysis buffer containing 1X Halt Protease Inhibitor (Thermo Fisher Cat. #78430) and stored frozen at -80°C. Frozen samples were shipped on dry ice to Eve Technologies Corp

(3415A - 3 Ave., NW, Calgary, AB T2N 0M4) to perform a standardized mouse cytokine array / chemokine array 31-Plex (MD31, Millipore MILLIPLEX). Samples were run in duplicate and the mean value was reported. The analytes tested for include Eotaxin, G-CSF, GM-CSF, IFNgamma, IL-1alpha, IL-1beta, IL-2, IL-3, IL-4, IL-5, IL-6, IL-7, IL-9, IL-10, IL-12 (p40), IL-12 (p70), IL-13, IL-15, IL-17A, IP-10, KC, LIF, LIX, MCP-1, M-CSF, MIG, MIP-1alpha, MIP-1beta, MIP-2, RANTES, TNFalpha, VEGF. Of the tested analytes, Eotaxin, G-CSF, GM-CSF, TNFa, IL1b, IL10, IL12p40, IL13, IL15, IL17, LIF, LIX, MCP-1, MIP-1b were below the limit of detection for the assay. IFNG, IL1a, IL2, IL3, IL4, IL5, IL7, IL9, IL12p70, KC, MIP-1a, MIP-2 were not significantly different between control and tumor samples.

Human/mouse cell assignment

Cells were aligned to a merged GRCh38/mm10 genome using Cell Ranger v3. Cells were then determined to be from mouse or human based on the frequency of reads aligning to the mouse genome with very low-quality cells with <200 genes (nFeature_RNA) filtered before estimating. Cells were called as mouse for all cells above the top elbow in the mouse read mapping frequency plot (>0.875 for Foxn1$^{nu/nu}$ data; >0.95 for MITRG data), human for all cells below the bottom elbow (<0.05 for Foxn1$^{nu/nu}$ data; <0.1 for MITRG data), and any other cells were discarded as doublets or poor quality. Any counts for GRCh38 genes in the cells called as mouse were removed from the expression matrix and vice versa for mm10 genes in human cells.

Quality control metrics

Cells for the Foxn1$^{nu/nu}$ cell type identification analysis were filtered to have between 500 and 2000 genes (nFeature_RNA) and <10% mitochondrial genome reads (percent.mito) in any retained cell. These cutoffs were selected based on analysis of violin plots for visual outliers. Putative microglia/astrocyte doublet clusters with marker gene co-expression were also removed from the Foxn1$^{nu/nu}$ microenvironment. This cell set was then used for subset myeloid and astrocyte analyses based on the cell type labels. Cells were further filtered for the myeloid analysis to have <5% percent.mito and low ribosomal expression (<10% of their transcriptome representing Rps and Rpl genes). An additional small cluster of putative microglia/astrocyte doublets was removed from the final astrocyte analysis. Cells for the MITRG analysis were filtered to have <20% percent.mtio. Doublets and empty gems (Negative) were also removed from the MITRG analysis based on MULTI-Seq barcoding label assignment from the R package deMULTIplex. Cell cycle signatures (S.Score and G2M.Score, determined by CellCycleScoring in Seurat) were regressed from the data for the 231BR analysis as well as the MITRG analysis before clustering and dimensionality reduction.

Clustering and differential expression

Main clustering and dimensionality reductions were performed in Seurat using the default Louvain and tSNE methods respectively. UMAP was used for dimensionality reductions in microglia subclustering analyses to better visualize global relationships. Some datasets were integrated using the mutual kNN algorithm adaptation in Seurat before these steps. Specifically, integration was performed on the Foxn1$^{nu/nu}$ full microenvironment and astrocyte analyses by sequencing batch (Con1:Met1, Con2:Con3, Met2:Met3). Integrated analyses used the “vst” selection method with nfeatures=2000 for FindVariableFeatures and dims=1:30 for FindIntegrationAnchors and IntegrateData. Differential expression analyses were run on the RNA assay in Seurat with FindAllMarkers/FindMarkers using the Wilcoxon rank sum test and adjusted *P* values represent the Bonferroni corrected values for all single-cell analyses. For all samples, cell types and states were assigned to clusters manually based on gene expression profiles.

GO term analysis and gene scoring

GO term analyses were performed using the MouseMine[71] web portal with list input for M. musculus with the default background population for mouse analyses and using the Enrichr portal[104,105] with a gene list input. Gene inputs for each condition included only genes considered differentially expressed with a Bonferroni adjusted P value < 0.05 from the Wilcoxon rank sum test. Specific GO terms were then selected from the Gene Ontology Enrichment section for biological_process with Holm-Bonferroni adjusted P value < 0.05 in MouseMine or the GO Biological Process 2018 list in Enrichr with unadjusted P value < 0.05. All gene scoring on single-cell data was performed in Seurat using the AddModuleScore function with default parameters. MG score gene list was taken directly as the Core MG list from Table S3 in Bowman et al, 2016[69]. Topic scores were determined for the MITRG mouse using the top 25 marker genes of each topic (ExtractTopFeatures with method = "poisson", options="min", and shared = FALSE), translated to human using the biomaRt package.

Latent Dirichlet Allocation, Topic model

To fit a topic model using Latent Dirichlet Allocation (LDA), we used the R package 'CountClust'[72] which was optimized for use on RNA-seq datasets. As input to our model, we provided a raw counts matrix containing all cells labeled as microglia and all detected genes from our Foxn1$^{nu/nu}$ dataset. The topic model was fit using the 'FitGoM' function, with a range of cluster numbers (K), and an error tol = 10. We chose the model with K = 15 since it achieved a relatively low value for the Bayesian Information Criterion

(BIC) and had enough resolution to provide topics with unique, biologically interpretable gene lists. Top gene markers for each topic were identified using the function ‘ExtractTopFeatures’ with method=’poisson’, options=’min’ and shared=TRUE for the marker heatmap (or shared = FALSE for gene scores).

Pseudotemporal Ordering of Cells

Monocle 3[106] was used for trajectory inference and pseudotemporal ordering of cells. For input, the final annotated Seurat object was converted to a Monocle 3 cds object using the SeuratWrappers function as.cell_data_set. The counts data matrix was then processed with the standard Monocle 3 pipeline using default parameters in the preprocess_cds and reduce_dimension functions. Clustering was performed with cluster_cells using resolution=3e-4 to maintain similar cluster assignments between Seurat and Monocle 3. The principal graph that defines the trajectory was constructed with the learn_graph function using one partition. To identify the root principal point for ordering cells, the helper function get_earliest_principal_node was used as defined in the Monocle 3 vignette, using D4_BL6 cells in our timepoint_strain metadata column. Pseudotemporal ordering was then performed using order_cells with root_pr_nodes=get_earliest_principal_node(cds). To display the pseudotime data on the original Seurat UMAP embeddings, the Monocle cds object was converted to a Seurat object with the Seurat function as.Seurat and the pseudotime metadata column of the resulting object was transferred to the original Seurat object using AddMetaData. The pseudotime results were then displayed as a feature plot using the plasma color palette from the viridis library.

Survival analysis

Our survival analysis was performed using the Brain-Met samples from Vareslija et al, 2018[94], based on the column header “M_” from their Github uploaded counts matrix (https://github.com/npriedig/jnci_2018/blob/master/brainMetPairs.salmon.cts.txt). This subset of the counts matrix was converted to log(cpm + 1) using the ‘cpm’ function in edgeR. This matrix was then merged with the clinical information from Table 1 of Vareslija et al, 2018[94], resulting in 20 total samples (samples "7M_RCS" and "19.2M_Pitt" were dropped, the first due to a lack of matching clinical data and the second due to sample replication). Our genes and signatures of interest, CD74, BST2, MHC-II genes ("HLA-DMA", "HLA-DMB", "HLA-DOA", "HLA-DOB", "HLA-DPA1", "HLA-DPB1", "HLA-DQA1", "HLA-DQA2", "HLA-DQB1", "HLA-DQB2", "HLA-DRA", "HLA-DRB1", "HLA-DRB3", "HLA-DRB4", "HLA-DRB5") and microglia ("P2RY12", "TMEM119", "GPR34", "CX3CR1", "CD81", "SELPLG") were converted to their Ensembl IDs using ‘mapIds’ with multiVals = ‘list’ from org.Hs.eg.db, and then added to the dataset as log(cpm +1) for the single genes, and the sum of the scaled data (z-scores) for multigene signatures. Survival analysis was then performed using the R package survminer, where each data stratification was made using ‘surv_cutpoint’ and ‘surv_categorize’ to identify an optimal split, and the KM curves were generated using ‘survfit’ in ‘ggsurvplot’.

Statistics and reproducibility

No statistical methods were used to pre-determine sample sizes, but sample sizes are similar to those reported in previous publications. Data distribution was assumed to be normal, but this was not formally tested. Mice with insufficient viable cell yield were excluded from analysis by flow cytometry. Where possible, experimental groups were randomized before initiation of experiments. Investigators were not blinded to allocation and experimental outcome except where otherwise indicated.

Data availability

RNA-seq data that support the findings of this study have been deposited in the Gene Expression Omnibus (GEO) under accession codes GSE147949 and GSE237386. Reference genome GRCh38/mm10 are available from Ensembl. MULTI-seq reads were processed according to the MULTI-seq protocol64 and available on GitHub (https://github.com/chris-mcginnis-ucsf/MULTIseq). Qptiff images were segmented in QuPath using StarDist and is available on GitHub (https://github. com/stardist/stardist). All other data are available from the corresponding author on reasonable request. Source data are provided with this paper.

References

1. Witzel, I., Oliveira-Ferrer, L., Pantel, K., Müller, V. & Wikman, H. Breast cancer brain metastases: Biology and new clinical perspectives. *Breast Cancer Res.* **18**, 1–9 (2016).
2. Ostrom, Q. T., Wright, C. H. & Barnholtz-Sloan, J. S. *Brain metastases: epidemiology*. *Handbook of Clinical Neurology* vol. 149 (Elsevier B.V., 2018).
3. Niikura, N. *et al.* Treatment outcomes and prognostic factors for patients with brain metastases from breast cancer of each subtype: a multicenter retrospective analysis. *Breast Cancer Res. Treat.* **147**, 103–112 (2014).
4. Brufsky, A. M. *et al.* Central nervous system metastases in patients with HER2-positive metastatic breast cancer: Incidence, treatment, and survival in patients from registHER. *Clin. Cancer Res.* **17**, 4834–4843 (2011).
5. Rostami, R., Mittal, S., Rostami, P., Tavassoli, F. & Jabbari, B. Brain metastasis in breast cancer: a comprehensive literature review. *Journal of Neuro-Oncology* (2016) doi:10.1007/s11060-016-2075-3.
6. Martin, A. M. *et al.* Immunotherapy and Symptomatic Radiation Necrosis in Patients With Brain Metastases Treated With Stereotactic Radiation. *JAMA Oncol.* **4**, 1123–1124 (2018).
7. Deeken, J. F. & Löscher, W. The blood-brain barrier and cancer: Transporters, treatment, and trojan horses. *Clin. Cancer Res.* **13**, 1663–1674 (2007).
8. Tosoni, A., Ermani, M. & Brandes, A. A. The pathogenesis and treatment of brain metastases: A comprehensive review. *Crit. Rev. Oncol. Hematol.* **52**, 199–215 (2004).
9. Hanisch, U. K. & Kettenmann, H. Microglia: Active sensor and versatile effector cells in the normal and pathologic brain. *Nature Neuroscience* (2007) doi:10.1038/nn1997.
10. Wolf, S. A., Boddeke, H. W. G. M. & Kettenmann, H. Microglia in Physiology and Disease. *Annu. Rev. Physiol.* **79**, 619–643 (2017).

11. Hammond, T. R., Robinton, D. & Stevens, B. Microglia and the Brain: Complementary Partners in Development and Disease. *Annu. Rev. Cell Dev. Biol.* **34**, 523–544 (2018).

12. Quail, D. F. & Joyce, J. A. The Microenvironmental Landscape of Brain Tumors. *Cancer Cell* **31**, 326–341 (2017).

13. Goldmann, T. *et al.* Origin, fate and dynamics of macrophages at central nervous system interfaces. *Nat. Immunol.* (2016) doi:10.1038/ni.3423.

14. Mrdjen, D. *et al.* High-Dimensional Single-Cell Mapping of Central Nervous System Immune Cells Reveals Distinct Myeloid Subsets in Health, Aging, and Disease. *Immunity* **48**, 380-395.e6 (2018).

15. Jordão, M. J. C. *et al.* Single-cell profiling identifies myeloid cell subsets with distinct fates during neuroinflammation. *Science (80-.).* (2019) doi:10.1126/science.aat7554.

16. Duchnowska, R. *et al.* Immune response in breast cancer brain metastases and their microenvironment: The role of the PD-1/PD-L axis. *Breast Cancer Res.* **18**, (2016).

17. Coniglio, S. J. *et al.* Microglial Stimulation of Glioblastoma Invasion Involves Epidermal Growth Factor Receptor (EGFR) and Colony Stimulating Factor 1 Receptor (CSF-1R) Signaling. *Mol. Med.* (2012) doi:10.2119/molmed.2011.00217.

18. Pyonteck, S. M. *et al.* CSF-1R inhibition alters macrophage polarization and blocks glioma progression. *Nat. Med.* **19**, 1264–1272 (2013).

19. Quail, D. F. *et al.* The tumor microenvironment underlies acquired resistance to CSF-1R inhibition in gliomas. *Science (80-.).* (2016) doi:10.1126/science.aad3018.

20. Yan, D. *et al.* Inhibition of colony stimulating factor-1 receptor abrogates microenvironment-mediated therapeutic resistance in gliomas. *Oncogene* (2017) doi:10.1038/onc.2017.261.

21. Qiao, S., Qian, Y., Xu, G., Luo, Q. & Zhang, Z. Long-term characterization of activated microglia/macrophages facilitating the development of experimental brain metastasis through intravital microscopic imaging. *J. Neuroinflammation* (2019) doi:10.1186/s12974018-1389-9.

22. Guldner, I. H. *et al.* CNS-Native Myeloid Cells Drive Immune Suppression in the Brain Metastatic Niche through Cxcl10. *Cell* 1–15 (2020) doi:10.1016/j.cell.2020.09.064.

23. Prinz, M. & Priller, J. Tickets to the brain: role of CCR2 and CX3CR1 in myeloid cell entry in the CNS. *J. Neuroimmunol.* **224**, 80–84 (2010).

24. Rojo, R. *et al.* Deletion of a Csf1r enhancer selectively impacts CSF1R expression and development of tissue macrophage populations. *Nat. Commun.* **10**, (2019).

25. Kettenmann, H., Hanisch, U.-K., Noda, M. & Verkhratsky, A. Physiology of Microglia. *Physiol. Rev.* (2011) doi:10.1152/physrev.00011.2010.

26. Dotiwala AK, McCausland C, Samra NS. Anatomy, Head and Neck: Blood Brain Barrier. In: StatPearls. StatPearls Publishing; 2023. Accessed November 27, 2023. http://www.ncbi.nlm.nih.gov/books/NBK519556/

27. Gernert M, Feja M. Bypassing the Blood–Brain Barrier: Direct Intracranial Drug Delivery in Epilepsies. Pharmaceutics. 2020;12(12):1134. doi:10.3390/pharmaceutics12121134

28. Cohen-Pfeffer JL, Gururangan S, Lester T, et al. Intracerebroventricular Delivery as a Safe, Long-Term Route of Drug Administration. Pediatric Neurology. 2017;67:23-35. doi:10.1016/j.pediatrneurol.2016.10.022

29. Fecci PE, Heimberger AB, Sampson JH. Immunotherapy for Primary Brain Tumors: No Longer a Matter of Privilege. Clinical Cancer Research. 2014;20(22):5620-5629. doi:10.1158/1078-0432.CCR-14-0832

30. Prinz M, Jung S, Priller J. Microglia Biology: One Century of Evolving Concepts. Cell. 2019;179(2):292-311. doi:10.1016/j.cell.2019.08.053

31. Vass K, Lassmann H, Wekerle H, Wisniewski HM. The distribution of Ia antigen in the lesions of rat acute experimental allergic encephalomyelitis. Acta Neuropathol. 1986;70(2):149-160. doi:10.1007/BF00691433

32. Prinz M, Masuda T, Wheeler MA, Quintana FJ. Microglia and Central Nervous System–Associated Macrophages—From Origin to Disease Modulation. Annu Rev Immunol. 2021;39:251-277. doi:10.1146/annurev-immunol-093019-110159

33. Gomez Perdiguero E, Klapproth K, Schulz C, et al. Tissue-resident macrophages originate from yolk-sac-derived erythro-myeloid progenitors. Nature. 2015;518(7540):547-551. doi:10.1038/nature13989

34. Ajami B, Bennett JL, Krieger C, Tetzlaff W, Rossi FMV. Local self-renewal can sustain CNS microglia maintenance and function throughout adult life. Nat Neurosci. 2007;10(12):1538-1543. doi:10.1038/nn2014

35. Colonna M, Butovsky O. Microglia Function in the Central Nervous System During Health and Neurodegeneration. Annual Review of Immunology. 2017;35(1):441-468. doi:10.1146/annurev-immunol-051116-052358

36. Madry C, Attwell D. Receptors, Ion Channels, and Signaling Mechanisms Underlying Microglial Dynamics. Journal of Biological Chemistry. 2015;290(20):12443-12450. doi:10.1074/jbc.R115.637157

37. Bachiller S, Jiménez-Ferrer I, Paulus A, et al. Microglia in Neurological Diseases: A Road Map to Brain-Disease Dependent-Inflammatory Response. Frontiers in Cellular Neuroscience. 2018;12. Accessed November 28, 2023. https://www.frontiersin.org/articles/10.3389/fncel.2018.00488

38. Sierra A, Gottfried-Blackmore AC, McEwen BS, Bulloch K. Microglia derived from aging mice exhibit an altered inflammatory profile. Glia. 2007;55(4):412-424. doi:10.1002/glia.20468

39. McGeer PL, McGeer EG. The inflammatory response system of brain: implications for therapy of Alzheimer and other neurodegenerative diseases. Brain Research Reviews. 1995;21(2):195-218. doi:10.1016/0165-0173(95)00011-9

40. Jurga AM, Paleczna M, Kuter KZ. Overview of General and Discriminating Markers of Differential Microglia Phenotypes. Front Cell Neurosci. 2020;14:198. doi:10.3389/fncel.2020.00198

41. Zindl CL, Chaplin DD. Tumor Immune Evasion. Science. 2010;328(5979):697-698. doi:10.1126/science.1190310

42. Vinay DS, Ryan EP, Pawelec G, et al. Immune evasion in cancer: Mechanistic basis and therapeutic strategies. Seminars in Cancer Biology. 2015;35:S185-S198. doi:10.1016/j.semcancer.2015.03.004

43. Kim SK, Cho SW. The Evasion Mechanisms of Cancer Immunity and Drug Intervention in the Tumor Microenvironment. Front Pharmacol. 2022;13:868695. doi:10.3389/fphar.2022.868695

44. Zhao XF, Alam MM, Liao Y, et al. Targeting Microglia Using Cx3cr1-Cre Lines: Revisiting the Specificity. eNeuro. 2019;6(4):ENEURO.0114-19.2019. doi:10.1523/ENEURO.0114-19.2019

45. Faust TE, Feinberg PA, O’Connor C, et al. A comparative analysis of microglial inducible Cre lines. Cell Reports. 2023;42(9):113031. doi:10.1016/j.celrep.2023.113031

46. Lehmann PV. The Fate of T Cells in the Brain. Am J Pathol. 1998;153(3):677-680.

47. Lochhead JJ, Yang J, Ronaldson PT, Davis TP. Structure, Function, and Regulation of the Blood-Brain Barrier Tight Junction in Central Nervous System Disorders. Front Physiol. 2020;11:914. doi:10.3389/fphys.2020.00914

48. Mostofa AGM, Punganuru SR, Madala HR, Al-Obaide M, Srivenugopal KS. The Process and Regulatory Components of Inflammation in Brain Oncogenesis. Biomolecules. 2017;7(2):34. doi:10.3390/biom7020034

49. Spiros A, Geerts H. A quantitative way to estimate clinical off-target effects for human membrane brain targets in CNS research and development. J Exp Pharmacol. 2012;4:53-61. doi:10.2147/JEP.S30808

50. Klein RS, Garber C, Howard N. Infectious immunity in the central nervous system and brain function. Nat Immunol. 2017;18(2):132-141. doi:10.1038/ni.3656

51. Piccio L, Rossi B, Scarpini E, et al. Molecular Mechanisms Involved in Lymphocyte Recruitment in Inflamed Brain Microvessels: Critical Roles for P-Selectin Glycoprotein Ligand-1 and Heterotrimeric Gi-Linked Receptors1. The Journal of Immunology. 2002;168(4):1940-1949. doi:10.4049/jimmunol.168.4.1940

52. Ransohoff RM, Kivisäkk P, Kidd G. Three or more routes for leukocyte migration into the central nervous system. Nat Rev Immunol. 2003;3(7):569-581. doi:10.1038/nri1130

53. Rickenbach C, Gericke C. Specificity of Adaptive Immune Responses in Central Nervous System Health, Aging and Diseases. Front Neurosci. 2022;15:806260. doi:10.3389/fnins.2021.806260

54. Schetters STT, Gomez-Nicola D, Garcia-Vallejo JJ, Van Kooyk Y. Neuroinflammation: Microglia and T Cells Get Ready to Tango. Frontiers in Immunology. 2018;8. Accessed December 4, 2023. https://www.frontiersin.org/articles/10.3389/fimmu.2017.01905

55. Kivisäkk P, Imitola J, Rasmussen S, et al. Localizing CNS immune surveillance: Meningeal APCs activate T cells during EAE. Ann Neurol. 2009;65(4):457-469. doi:10.1002/ana.21379

56. van Zwam M, Huizinga R, Melief MJ, et al. Brain antigens in functionally distinct antigen-presenting cell populations in cervical lymph nodes in MS and EAE. Journal of molecular medicine (Berlin, Germany). 2009;87:273-286. doi:10.1007/s00109-008-0421-4

57. Lauko A, Rauf Y, Ahluwalia MS. Medical management of brain metastases. Neurooncol Adv. 2020;2(1):vdaa015. doi:10.1093/noajnl/vdaa015

58. Patel AJ, Suki D, Hatiboglu MA, Rao VY, Fox BD, Sawaya R. Impact of surgical methodology on the complication rate and functional outcome of patients with a single brain metastasis. Journal of Neurosurgery. 2015;122(5):1132-1143. doi:10.3171/2014.9.JNS13939

59. Hong A, Fogarty G, Dolven-Jacobsen K, Thompson J, Middleton M, Al. E. Adjuvant whole-brain radiation therapy compared with observation after local treatment of melanoma brain metastases: a multicenter,

randomized phase III trial. Journal of Clinical Oncology. 2019;37(33). Accessed November 29, 2023. https://ora.ox.ac.uk/objects/uuid:2099f136-5939-45ab-8bbf-4ca44579dc67

60. Mahajan A, Ahmed S, McAleer MF, et al. Post-operative stereotactic radiosurgery versus observation for completely resected brain metastases: a single-centre, randomised, controlled, phase 3 trial. The Lancet Oncology. 2017;18(8):1040-1048. doi:10.1016/S1470-2045(17)30414-X

61. The Nobel Prize in Physiology or Medicine 2018. NobelPrize.org. Accessed December 4, 2023. https://www.nobelprize.org/prizes/medicine/2018/press-release/

62. Patel RR, Verma V, Miller AB, et al. Exclusion of patients with brain metastases from cancer clinical trials. Neuro Oncol. 2020;22(4):577-579. doi:10.1093/neuonc/noz246

63. Clinical Trials Using Enadenotucirev-expressing Anti-CD40 Agonistic Monoclonal Antibody NG-350A - NCI. Published June 13, 2017. Accessed December 4, 2023. https://www.cancer.gov/research/participate/clinical-trials/intervention/enadenotucirev-expressing-anti-cd40-agonistic-monoclonal-antibody-ng-350a

64. Clinical Trials Using Fc-engineered Anti-CD40 Agonist Antibody 2141-V11 - NCI. Published June 13, 2017. Accessed December 4, 2023. https://www.cancer.gov/research/participate/clinical-trials/intervention/fc-engineered-anti-cd40-agonist-antibody-2141-v11

65. Bos, P. D. *et al.* Genes that mediate breast cancer metastasis to the brain. *Nature* (2009) doi:10.1038/nature08021.

66. Lorger, M. & Felding-Habermann, B. Capturing changes in the brain microenvironment during initial steps of breast cancer brain metastasis. *Am. J. Pathol.* **176**, 2958–2971 (2010).

67. Kienast, Y. *et al.* Real-time imaging reveals the single steps of brain metastasis formation. *Nat. Med.* **16**, 116–122 (2010).

68. Valiente, M. *et al.* Serpins promote cancer cell survival and vascular Co-option in brain metastasis. *Cell* (2014) doi:10.1016/j.cell.2014.01.040.

69. Bowman, R. L. *et al.* Macrophage Ontogeny Underlies Differences in Tumor-Specific Education in Brain Malignancies. *Cell Rep.* **17**, (2016).

70. O'Flanagan, C. H. *et al.* Dissociation of solid tumor tissues with cold active protease for single-cell RNA-seq minimizes conserved collagenase-associated stress responses. *Genome Biol.* **20**, 1–13 (2019).

71. Motenko, H., Neuhauser, S. B., O'Keefe, M. & Richardson, J. E. MouseMine: a new data warehouse for MGI. *Mamm. Genome* **26**, 325–330 (2015).

72. Dey, K. K., Hsiao, C. J. & Stephens, M. Visualizing the structure of RNA-seq expression data using grade of membership models. *PLoS Genet.* **13**, 1–23 (2017).

73. Mathys, H. *et al.* Temporal Tracking of Microglia Activation in Neurodegeneration at Single-Cell Resolution. *Cell Rep.* **21**, 366–380 (2017).

74. Hammond, T. R. *et al.* Single-Cell RNA Sequencing of Microglia throughout the Mouse Lifespan and in the Injured Brain Reveals Complex Cell-State Changes. *Immunity* **50**, 253-271.e6 (2019).

75. Ochocka, N. *et al.* Single-cell RNA sequencing reveals functional heterogeneity of glioma-associated brain macrophages. *Nat. Commun.* **12**, 1–14 (2021).

76. Ivashkiv, L. B. & Donlin, L. T. Regulation of type i interferon responses. *Nat. Rev. Immunol.* **14**, 36–49 (2014).

77. Keren-Shaul, H. *et al.* A Unique Microglia Type Associated with Restricting Development of Alzheimer's Disease. *Cell* **169**, 1276-1290.e17 (2017).

78. Blasius, A. L. *et al.* Bone Marrow Stromal Cell Antigen 2 Is a Specific Marker of Type I IFN-Producing Cells in the Naive Mouse, but a Promiscuous Cell Surface Antigen following IFN Stimulation. *J. Immunol.* (2006) doi:10.4049/jimmunol.177.5.3260.

79. Neil, S. J. D., Zang, T. & Bieniasz, P. D. Tetherin inhibits retrovirus release and is antagonized by HIV-1 Vpu. *Nature* (2008) doi:10.1038/nature06553.

80. Ting, J. P. Y. & Trowsdale, J. Genetic control of MHC class II expression. *Cell* (2002) doi:10.1016/S0092-8674(02)00696-7.

81. Schröder, B. The multifaceted roles of the invariant chain CD74 — More than just a chaperone. *Biochim. Biophys. Acta - Mol. Cell Res.* **1863**, 1269–1281 (2016).

82. Butovsky, O. *et al.* Identification of a unique TGF-β-dependent molecular and functional signature in microglia. *Nat. Neurosci.* (2014) doi:10.1038/nn.3599.

83. Gosselin, D. *et al.* An environment-dependent transcriptional network specifies human microglia identity. *Science (80-.).* (2017) doi:10.1126/science.aal3222.

84. Watanabe, H., Numata, K., Ito, T., Takagi, K. & Matsukawa, A. Innate immune response in Th1- and Th2-dominant mouse strains. *Shock* (2004) doi:10.1097/01.shk.0000142249.08135.e9.

85. Stanley, E. R. *et al.* Biology and action of colony-stimulating factor-1. *Mol. Reprod. Dev.* **46**, (1997).

86. Tokunaga, R. *et al.* CXCL9, CXCL10, CXCL11/CXCR3 axis for immune activation – A target for novel cancer therapy. *Cancer Treatment Reviews* vol. 63 (2018).

87. Aldinucci, D. & Colombatti, A. The inflammatory chemokine CCL5 and cancer progression. *Mediators Inflamm.* **2014**, (2014).

88. Elmore, M. R. P. *et al.* Replacement of microglia in the aged brain reverses cognitive, synaptic, and neuronal deficits in mice. *Aging Cell* (2018) doi:10.1111/acel.12832.

89. Spangenberg, E. *et al.* Sustained microglial depletion with CSF1R inhibitor impairs parenchymal plaque development in an Alzheimer's disease model. *Nat. Commun.* (2019) doi:10.1038/s41467-019-11674-z.

90. Munro, D. A. D. *et al.* CNS macrophages differentially rely on an intronic Csf1r enhancer for their development. *Development* **147**, dev194449 (2020).

91. McQuade, A. *et al.* Development and validation of a simplified method to generate human microglia from pluripotent stem cells. *Mol. Neurodegener.* (2018) doi:10.1186/s13024018-0297-x.

92. Hasselmann, J. *et al.* Development of a Chimeric Model to Study and Manipulate Human Microglia In Vivo. *Neuron* (2019) doi:10.1016/j.neuron.2019.07.002.

93. Rongvaux, A. *et al.* Development and function of human innate immune cells in a humanized mouse model. *Nat. Biotechnol.* (2014) doi:10.1038/nbt.2858.

94. Varešlija, D. *et al.* Transcriptome characterization of matched primary breast and brain metastatic tumors to detect novel actionable targets. *J. Natl. Cancer Inst.* **111**, 388–398 (2019).

95. Marsh, S.E., Walker, A.J., Kamath, T. et al. Dissection of artifactual and confounding glial signatures by single-cell sequencing of mouse and human brain. Nat Neurosci 25, 306–316 (2022).

96. Ocañas SR, Pham KD, Blankenship HE, Machalinski AH, Chucair-Elliott AJ, Freeman WM. Minimizing the Ex Vivo Confounds of Cell-Isolation Techniques on Transcriptomic and Translatomic Profiles of Purified Microglia. eNeuro. 2022 Mar 28;9(2):ENEURO.0348-

97. Klemm, F. *et al.* Compensatory CSF2-driven macrophage activation promotes adaptive resistance to CSF1R inhibition in breast-to-brain metastasis. *Nature Cancer* vol. 2
(Springer US, 2021).

98. Huang, Y. *et al.* Repopulated microglia are solely derived from the proliferation of residual microglia after acute depletion. *Nat. Neurosci.* **21**, 530–540 (2018).

99. Lund, H. *et al.* Competitive repopulation of an empty microglial niche yields functionally distinct subsets of microglia-like cells. *Nat. Commun.* **9**, (2018).

100. Bruttger, J. *et al.* Genetic Cell Ablation Reveals Clusters of Local Self-Renewing Microglia in the Mammalian Central Nervous System. *Immunity* **43**, 92–106 (2015).

101. Han, J., Harris, R. A. & Zhang, X. M. An updated assessment of microglia depletion: Current concepts and future directions. *Mol. Brain* **10**, 1–8 (2017).

102. Campbell, J. P., Merkel, A. R., Masood-Campbell, S. K., Elefteriou, F. & Sterling, J. A. Models of Bone Metastasis. *J. Vis. Exp.* (2012) doi:10.3791/4260.

103. McGinnis, C. S. *et al.* MULTI-seq: sample multiplexing for single-cell RNA sequencing using lipid-tagged indices. *Nat. Methods* (2019) doi:10.1038/s41592-019-0433-8.

104. Chen, E. Y. *et al.* Enrichr: interactive and collaborative HTML5 gene list enrichment analysis tool. *BMC Bioinformatics* **14**, 128 (2013).

105. Kuleshov, M. V *et al.* Enrichr: a comprehensive gene set enrichment analysis web server 2016 update. *Nucleic Acids Res.* **44**, W90-7 (2016).

106. Cao, J., Spielmann, M., Qiu, X. et al. The single-cell transcriptional landscape of mammalian organogenesis. Nature 566, 496–502 (2019). https://doi.org/10.1038/s41586-019-0969-x

APPENDIX A: SUPPLEMENTARY TABLES

Table S1. Marker genes of each cell type in the 231BR-Foxn1$^{nu/nu}$ scRNA-seq data set.

Table S2. Marker genes of astrocytes from control and metastatic brain in the 231BRFoxn1$^{nu/nu}$ scRNA-seq data set.

Table S3. Gene lists for gene scoring analyses.

Table S4. Marker genes of myeloid cell types and microglia from control and metastatic brain in the 231BR-Foxn1$^{nu/nu}$ scRNA-seq data set.

Table S5. Top genes comprising each topic upregulated by microglia in BCBM in the 231BR-Foxn1$^{nu/nu}$ scRNA-seq data set.

Table S6. Marker genes of myeloid cell types and microglia from control and metastatic brain in the humanized 231BR-MITRG scRNA-seq data set.

Supplementary tables available at the following URL:

https://static-content.springer.com/esm/art%3A10.1038%2Fs41556-023-01273-y/MediaObjects/41556_2023_1273_MOESM4_ESM.xlsx